JOURNAL OF COMPUTATIONAL PHYSICS **144,** 662–709 (1998)
ARTICLE NO. CP986010

High-Order Finite-Difference Schemes for Numerical Simulation of Hypersonic Boundary-Layer Transition

Xiaolin Zhong

Department of Mechanical and Aerospace Engineering, 46-147C, Engineering IV Building, University of California, Los Angeles, California 90095
E-mail: xiaolin@seas.ucla.edu

Received August 28, 1997; revised April 17, 1998

Direct numerical simulation (DNS) has become a powerful tool in studying fundamental phenomena of laminar-turbulent transition of high-speed boundary layers. Previous DNS studies of supersonic and hypersonic boundary layer transition have been limited to perfect-gas flow over flat-plate boundary layers without shock waves. For hypersonic boundary layers over realistic blunt bodies, DNS studies of transition need to consider the effects of bow shocks, entropy layers, surface curvature, and finite-rate chemistry. It is necessary that numerical methods for such studies are robust and high-order accurate both in resolving wide ranges of flow time and length scales and in resolving the interaction between the bow shocks and flow disturbance waves. This paper presents a new high-order shock-fitting finite-difference method for the DNS of the stability and transition of hypersonic boundary layers over blunt bodies with strong bow shocks and with (or without) thermo-chemical nonequilibrium. The proposed method includes a set of new upwind high-order finite-difference schemes which are stable and are less dissipative than a straightforward upwind scheme using an upwind-bias grid stencil, a high-order shock-fitting formulation, and third-order semi-implicit Runge–Kutta schemes for temporal discretization of stiff reacting flow equations. The accuracy and stability of the new schemes are validated by numerical experiments of the linear wave equation and nonlinear Navier–Stokes equations. The algorithm is then applied to the DNS of the receptivity of hypersonic boundary layers over a parabolic leading edge to freestream acoustic disturbances.

1. INTRODUCTION

The prediction of laminar-turbulent transition of hypersonic boundary layers is critical to the accurate calculations of drag and thermal loads to hypersonic vehicles [1]. Figure 1 shows a schematic of a generic hypersonic lifting vehicle with boundary-layer transition.

0021-9991/98 $25.00

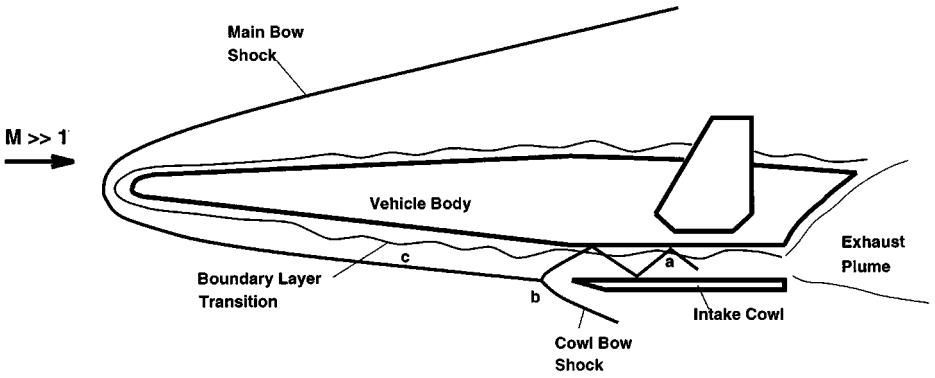

FIG. 1. A schematic of a generic hypersonic lifting vehicle with boundary-layer transition.

In general, transition is a result of nonlinear response of laminar boundary layers to forcing disturbances [2, 3], which can originate from freestream acoustic, turbulent, or entropy disturbances, or from disturbances induced by surface roughness or surface vibrations. In an environment with small initial disturbances, the path to transition consists of three stages: (1) receptivity, (2) linear eigenmode growth, and (3) nonlinear breakdown to turbulence. The receptivity process [4] converts the environmental disturbances into boundary-layer instability waves, and provides important initial conditions of amplitude, frequency, and phase for boundary-layer instability waves [5]. The second stage is the linear eigenmode growth of boundary-layer instability waves. The relevant wave modes for hypersonic boundary layers are the first mode and second (acoustic) mode [6], the Görtler instabilities [7] over concave surfaces, and the three-dimensional cross flow instabilities [8]. It has been shown [6, 9] that both the first and the second mode instabilities are simultaneously present in hypersonic boundary layers where the second mode is most unstable at high Mach numbers. The third stage is the breakdown of linear instability waves and transition to turbulence after the linear growth of instability waves reaches certain magnitudes [10].

Compared with low-speed boundary layers, the transition of hypersonic boundary layers over blunt bodies is affected by the additional effects of bow-shock interactions, nose bluntness, entropy layer instabilities, and thermo-chemical nonequilibrium at high temperatures. Figure 2 shows a schematic of wave fields in a hypersonic flow induced by freestream disturbances. Kovasznay [11] showed that weak disturbance waves in compressible flow can be decomposed into three independent acoustic, entropy, and vorticity modes. Freestream disturbances are processed by the bow shock before entering the boundary layer. Irrespective of the nature of the freestream disturbance modes, their interaction with the bow shock always generates all three types of wave modes, which propagate downstream and interact with the boundary layer over the body surface. The boundary layer also generates reflected acoustic waves impinging on the shock from behind and generating further disturbances to the shock. In addition, an entropy layer is created by the curved bow shock. The swallowing of the entropy layer by the boundary layer has been shown to have strong effects on the stability and transition of the boundary layer downstream [12] further downstream. Therefore, it is necessary to include the effects of the bow shock in the studies of hypersonic boundary-layer transition.

This paper is concerned with finite-difference methods for the DNS of stability and transition of hypersonic boundary layers over blunt bodies. In DNS studies, boundary-layer

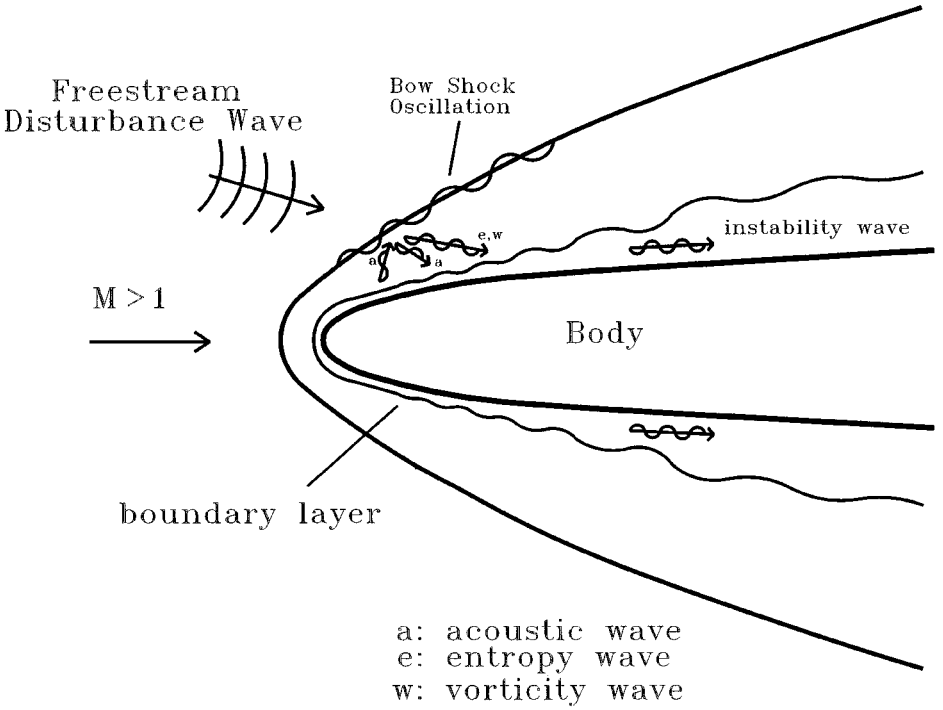

FIG. 2. A schematic of the wave field of hypersonic boundary layer receptivity to freestream disturbances.

transition [13] is simulated by numerically solving the three-dimensional Navier–Stokes equations for the development of disturbance waves in the boundary layers. Highly accurate numerical methods are needed in order to resolve a wide range of flow time and length scales. Due to the advances in numerical methods and rapid increases in memory capacity and computational speeds of available computers, DNS has become a powerful tool in the study of flow phenomena of the stability and transition of boundary layers [13], especially in the DNS of incompressible boundary layer stability and transition [14–21]. For compressible boundary layers over a flat plate, Erlebacher *et al.* [22, 23] studied the secondary instability mechanism by temporal and spatial simulations. Thumm *et al.* [24] and Eibler and Bestek [25] performed spatial DNS of the oblique mode breakdown in supersonic boundary layers over flat plates. Adams and Kleiser [26] and Guo *et al.* [27] studied the subharmonic breakdown process at a freestream Mach number of 4.5 by temporal and spatial simulations. Pruett *et al.* [28, 29] conducted temporal and spatial DNS studies of laminar breakdown in high-speed axisymmetric boundary layers over a hollow cylinder and a sharp cone.

These previous DNS studies of supersonic boundary layers were limited to perfect gas flow over flat-plate boundary layers without shock waves. For hypersonic boundary layers over realistic blunt bodies, the DNS studies need to consider the effects of bow shocks, entropy layers, surface curvature, and finite-rate chemistry. The numerical methods for such studies need to be robust, high-order accurate, and able to solve the bow shock oscillations. This paper presents new high-order upwind finite-difference shock-fitting schemes for the direct numerical simulation of hypersonic flows with strong bow shocks and with (or without) stiff chemical source terms. A new set of upwind high-order finite-difference schemes is proposed for the accurate and stable spatial discretization of flow equations

behind the bow shocks. A shock-fitting formulation is used so that the high-order schemes can be used to compute unsteady shock motions and its interaction with the transient flow without introducing spurious numerical oscillations in the solutions. The resulting system of ordinary differential equations is advanced in time using third-order semi-implicit Runge–Kutta schemes [30] for stiff reacting flow equations or by regular explicit Runge–Kutta schemes for non-stiff equations. These three aspects of the numerical method are discussed further below.

High-Order Upwind Finite-Difference Schemes

The traditional numerical methods for the DNS of transitional and turbulent flows have been the spectral methods because of their high accuracies. But the applications of the spectral methods have been limited to flows in simple domains. Several alternative numerical methods have been used for DNS of transitional and turbulent flows in general geometries. Examples are the spectral element methods [31], high-order compact (Padé) finite-difference methods [32], and high-order non-compact (explicit) finite-difference methods [18].

Finite-difference methods have recently received much attention for the DNS of transitional and turbulent flows [17, 18, 26, 29, 32] because they can be easily applied to complex geometries. Finite-difference schemes include both traditional explicit schemes and compact [32] schemes. High-order schemes are required because traditional second-order schemes do not have an adequate accuracy level for the direct numerical simulation. Most high-order finite-difference methods used in direct numerical simulation are central difference schemes [29, 32] which introduce only phase errors but no dissipative errors in numerical solutions. The drawback of central schemes is that they are not robust enough for convection dominated hypersonic flow simulations. Extra filtering procedures, which are equivalent to adding numerical dissipation in an ad hoc manner, are needed in order to stabilize the computations and control the aliasing errors. For example, central difference schemes of fourth order or higher are unstable when they are coupled with high-order boundary schemes using one-sided finite-difference approximations [29, 33]. Carpenter *et al.* [33] showed that for a sixth-order inner central compact scheme, only a third-order boundary scheme can be used without introducing instability. This results in a globally fourth-order accurate scheme even though the inner scheme is sixth-order accurate.

On the other hand, Rai and Moin [18] showed that upwind-bias schemes are very robust even when they are made high-order accurate. They used a spatially fifth-order upwind finite-difference scheme using an upwind-bias stencil for the Navier–Stokes equations. The numerical dissipation in the upwind-bias schemes is enough to control the aliasing errors. In recent years, many other upwind high-order schemes have also been developed. Tolstykh [34] proposed a fifth-order compact upwind scheme for moisture transport equation in atmosphere. Christie [35] proposed a fourth-order compact upwind scheme because the standard central compact schemes break down in convection dominated problems. Zingg *et al.* [36] tested the accuracy of a fifth-order explicit upwind finite-difference scheme with built-in filtering terms in a central grid stencil for linear wave propagation problems. Sjögreen [37] used explicit numerical damping to stabilize high-order finite-difference equations for the Navier–Stokes equations. Adams and Shariff [38] proposed fifth-order upwind compact schemes with spectral-like resolution using central grid stencils for the direct numerical simulation of shock-turbulence interaction.

This paper presents a family of upwind compact and explicit finite-difference schemes of third, fifth, and seventh-order and their stable high-order boundary schemes for the DNS

of hypersonic boundary-layer transition. The main idea is to derive the upwind schemes so that the dissipative errors are smaller than the dispersive errors inherent in equivalent central schemes and are large enough to stabilize high-order inner schemes coupled with boundary closure schemes. Fourier analysis is used to analyze the dissipation and phase errors, and an asymptotic stability analysis is used to determine the stability of the inner schemes coupled with boundary conditions. Specifically, central grid stencils are used for the upwind schemes with adjustable built-in numerical dissipation. The orders of accuracy of the upwind schemes are one-order lower than the maximum orders the central stencils can achieve so that there is an adjustable coefficient in the leading dissipative truncation term. The free parameters are then determined so that the resulting upwind schemes satisfy dissipation-error and stability conditions. The current upwind schemes are similar to the upwind schemes of Zingg *et al.* [36] and those of Adams and Shariff [38]. But they are more general and systematic in derivation and analysis.

High-Order Shock-Fitting Method

For the DNS of hypersonic flow over blunt bodies, high-order linear schemes cannot be used for grid points across the bow shock fronts with steep gradients because spurious numerical oscillations are generated at the shocks. Many high-resolution shock capturing schemes, such as the TVD and ENO [39] schemes, have been developed to capture shock waves as part of the numerical solutions without numerical oscillations. These shock capturing schemes are adequate for aerodynamic calculations, but they are not accurate enough for DNS studies, where short wave-length shock/disturbance interactions need to be resolved with high accuracy.

For DNS of hypersonic boundary layers, the bow shocks can be treated as a computational boundary using the shock-fitting method [40]. The use of the shock-fitting method makes it possible to apply high-order linear schemes for spatial discretization of the flow equations behind the bow shocks. Hussaini *et al.* [40] used the shock-fitting spectral method to simulate shock/turbulent interaction. Cai [41] used a shock-fitting method to compute two-dimensional detonation waves. The interactions between the bow shocks and disturbance waves are resolved by the shock-fitting method without generating numerical spurious oscillations. This paper presents a high-order shock-fitting formulation for the DNS of three-dimensional hypersonic boundary layers with unsteady bow shocks. The current formulation is simple because the relations across the shock are consistent with conservative flux and its Jacobian used in computing the conservation equations behind the shocks.

Semi-implicit Runge–Kutta Schemes

The perfect gas assumption commonly used in direct numerical simulation becomes inaccurate for practical hypersonic flows because flow temperatures rise significantly across the bow shocks. As a result, the gas between the shock and the body surface becomes thermally excited and chemically reacting. The temporal integration calculations are often stiff for such transient reacting flow simulations. We have developed [30] a set of third-order semi-implicit Runge–Kutta schemes for the high-order temporal discretization of the flow equations with stiff thermo-chemical nonequilibrium source terms. The third-order semi-implicit Runge–Kutta schemes are able to compute stiff reactive flow equations with third-order temporal accuracy and are unconditionally stable for the stiff terms. On the other

hand, for the DNS of non-reacting perfect-gas hypersonic flows at relative low Reynolds numbers, the semi-implicit Runge–Kutta schemes are replaced by simpler explicit Runge–Kutta schemes, such as the low-storage Runge–Kutta schemes of Williamson [42].

2. EQUATIONS

The governing equations for the DNS of hypersonic boundary layer transition are the three-dimensional Navier–Stokes equations, which can be written in the following conservation-law form in the Cartesian coordinates,

$$\frac{\partial U}{\partial t} + \frac{\partial F_j}{\partial x_j} + \frac{\partial F_{vj}}{\partial x_j} = W, \tag{1}$$

where U, F_j, and F_{vj} are the vectors of flow variables, convective flux, and viscous flux in the jth spatial direction respectively, i.e.,

$$U = \{\rho_m, \rho u_1, \rho u_2, \rho u_3, e\} \tag{2}$$

$$F_j = \begin{Bmatrix} \rho_m u_j \\ \rho u_1 u_j + p\delta_{1j} \\ \rho u_2 u_j + p\delta_{2j} \\ \rho u_3 u_j + p\delta_{3j} \\ (e+p)u_j \end{Bmatrix} \tag{3}$$

$$F_{vj} = \begin{Bmatrix} 0 \\ \tau_{1j} \\ \tau_{2j} \\ \tau_{3j} \\ \tau_{jk}u_k - q_j \end{Bmatrix}. \tag{4}$$

In Eq. (1), $W = W(U)$, is the source terms introduced by the thermo-chemical nonequilibrium processes. The specific formulas for the source terms are determined by physical models used for the nonequilibrium processes. Details of a five-species air model for hypersonic flows can be found in [43].

In this paper, only a special case of perfect-gas hypersonic flow is considered in detail for the purpose of presenting and testing the numerical methods. The numerical methods can be extended to nonequilibrium flow easily. For perfect gas flow, the source term **W** vanishes and the equation of state and the transport equations are

$$p = \rho RT \tag{5}$$

$$e = \rho\left(c_v T + \frac{1}{2}u_k u_k\right) \tag{6}$$

$$\tau_{ij} = \mu\left(\frac{\partial u_i}{\partial x_j} + \frac{\partial u_j}{\partial x_i}\right) - \lambda\frac{\partial u_k}{\partial x_k}\delta_{ij} \tag{7}$$

$$q_j = -\kappa\frac{\partial T}{\partial x_j}, \tag{8}$$

where R is the gas constant. The specific heats c_p and c_v are assumed to be constants with a given ratio of specific heats γ. The viscosity coefficient μ can be calculated by Sutherland's

law in the form

$$\mu = \mu_r \left(\frac{T}{T_0}\right)^{3/2} \frac{T_r + T_s}{T + T_s} \tag{9}$$

and λ is assumed to be $-2\mu/3$. The heat conductivity coefficient κ can be computed through a constant Prandtl number Pr.

3. UPWIND SCHEMES USING CENTERED GRID STENCILS

The governing equation (1) is discretized using the method of lines by separate spatial and temporal discretizations. The main difficulty in the spatial discretization is the numerical instability of high-order schemes for discretizing the inviscid convective flux terms. High-order central finite-difference schemes can be used for the viscous flux terms. This paper derives a family of finite-difference high-order upwind compact and explicit schemes for the discretization of convective terms for the direct numerical simulations of hypersonic boundary layers. The model equation of the inviscid Euler equations in deriving the upwind schemes is the linear wave equation

$$\frac{\partial u}{\partial t} + c\frac{\partial u}{\partial x} = 0, \qquad a \le x \le b, \tag{10}$$

where $c > 0$. Downwind schemes for $c < 0$ can be easily obtained from upwind schemes. In spatial discretization of Eq. (10), the general compact and explicit finite-difference approximation for $\partial u/\partial x$ located at the ith grid point can be written as [32, 38]

$$\sum_{k=-M+M_0+1}^{M_0} b_{i+k} u'_{i+k} = \frac{1}{h} \sum_{k=-N+N_0+1}^{N_0} a_{i+k} u_{i+k}, \tag{11}$$

where uniform grids with grid spacing of h are assumed, and u'_{i+k} is the numerical approximation of $\partial u/\partial x$ located at the $(i+k)$th grid point. On the right hand side of the equation, a total of N grid points are used with N_0 points biased with respect to the base point i. A similar grid combination of M and M_0 is used on the left hand side of the equation. In this paper, a scheme using this grid combination is termed the N-N_0-M-M_0 scheme, which includes both compact and explicit schemes as its special cases.

This paper considers a family of upwind compact and explicit high-order finite-difference methods using central grid stencils, i.e.,

$$N = 2N_0 + 1 \tag{12}$$

$$M = 2M_0 + 1. \tag{13}$$

The coefficients a_{i+k} and b_{i+k} of the upwind schemes are determined such that the order of the schemes is one order lower than the maximum achievable order for the central stencil, i.e., the orders of the upwind schemes are always odd integers of $p = 2(N_0 + M_0) - 1$. As a result, there is a free parameter α in the coefficients a_{i+k} and b_{i+k}. The free parameter is set to be the coefficient of the leading truncation term which is a derivative even order, i.e.,

$$\sum_{k=-M_0}^{M_0} b_{i+k} u'_{i+k} = \frac{1}{h} \sum_{k=-N_0}^{N_0} a_{i+k} u_{i+k} - \frac{\alpha}{(p+1)!} h^p \left(\frac{\partial u^{p+1}}{\partial^{p+1} x}\right)_i + \cdots, \tag{14}$$

where $p = 2(N_0 + M_0) - 1$, and α is the free parameter. All schemes with nonzero α are pth order accurate, and they are central schemes of $(p+1)$th order when $\alpha = 0$. The choice of α is not unique, and it has effects mainly on the magnitudes of numerical dissipation and on the stability of the schemes. The specific value of α for an upwind scheme is chosen to be large enough to stabilize the high-order upwind inner scheme when it is coupled with stable boundary closure schemes, and to be small enough so that the dissipation errors are comparable to the dispersion errors of the inner scheme.

The detailed expressions of the fifth-order upwind compact and explicit upwind schemes are derived below. Only three-point compact schemes ($M = 3$) are considered in order to maintain the computational efficiency of the schemes. The corresponding third- and seventh-order schemes can be derived similarly, and they are listed in the Appendix.

Fifth-Order Upwind Compact Schemes

A fifth-order compact scheme can be obtained using a 5-2-3-1 grid stencil as

$$b_{i-1}u'_{i-1} + b_i u'_i + b_{i+1}u'_{i+1} = \frac{1}{h}\sum_{k=-2}^{2} a_{i+k}u_{i+k} - \frac{\alpha}{6!}h^5\left(\frac{\partial u^6}{\partial^6 x}\right)_i + \cdots, \tag{15}$$

where

$$\begin{aligned} a_{i\pm2} &= \pm\frac{5}{3} + \frac{5}{6}\alpha, & b_{i\pm1} &= 20 \pm \alpha \\ a_{i\pm1} &= \pm\frac{140}{3} + \frac{20}{3}\alpha & & \\ a_i &= -15\alpha, & b_i &= 60. \end{aligned}$$

These schemes are fifth-order upwind compact schemes when $\alpha < 0$, and they reduce to the sixth-order central scheme when $\alpha = 0$. The specific value of α for an upwind scheme is determined based on the analyses on the dissipation errors and stability of the inner scheme with boundary conditions.

The dissipation and dispersive errors of the high-order upwind schemes are analyzed using the Fourier analysis when they are applied to Eq. (10) with a periodic boundary condition. The trial solution is

$$u = v(t)\, e^{i\omega x/h}. \tag{16}$$

The exact derivative of the trial solution is

$$\frac{\partial u}{\partial x} = \frac{i\omega}{h}u. \tag{17}$$

Applying the trial function to a finite-difference scheme given by Eq. (14) leads to

$$\frac{\partial u}{\partial x} = \frac{i\omega_1}{h}u, \tag{18}$$

where

$$\omega_1 = -i\frac{\sum_{k=-N_0}^{N_0} a_{i+k}\, e^{ik\omega}}{\sum_{k=-M_0}^{M_0} b_{i+k}\, e^{ik\omega}}. \tag{19}$$

The dimensionless dispersive (phase) and dissipative errors of using the finite-difference scheme to approximate the derivative in the linear wave equation are represented by the real and imaginary parts of $\omega_1 - \omega$, i.e.,

$$\text{Phase Errors} = \text{Real}(\omega_1 - \omega) \tag{20}$$

$$\text{Dissipation Errors} = \text{Im}(\omega_1), \tag{21}$$

where the errors are functions of the dimensionless parameter ω.

Figure 3 shows the dispersion and dissipation errors of three fifth-order compact 5-2-3-1 schemes with α at 0, -1, and -2. The figure shows that compact upwind schemes with different values of α have different phase errors as shown by the solid lines in the figures because of the rational formulas used in the compact schemes. The dissipation errors of the compact schemes increase as α increases. For α satisfying

$$-1 \leq \alpha \leq 0 \tag{22}$$

the dissipation errors of the upwind compact schemes are smaller or comparable to the corresponding phase errors. Therefore, the value of α satisfying (22) is considered to satisfy the dissipation condition. The smaller is the magnitude of α, the smaller are the dissipation errors of the upwind compact schemes.

Though very small or zero values of α lead to a scheme with very small or no dissipation, when α is too small, a compact 5-2-3-1 scheme is not stable when the inner

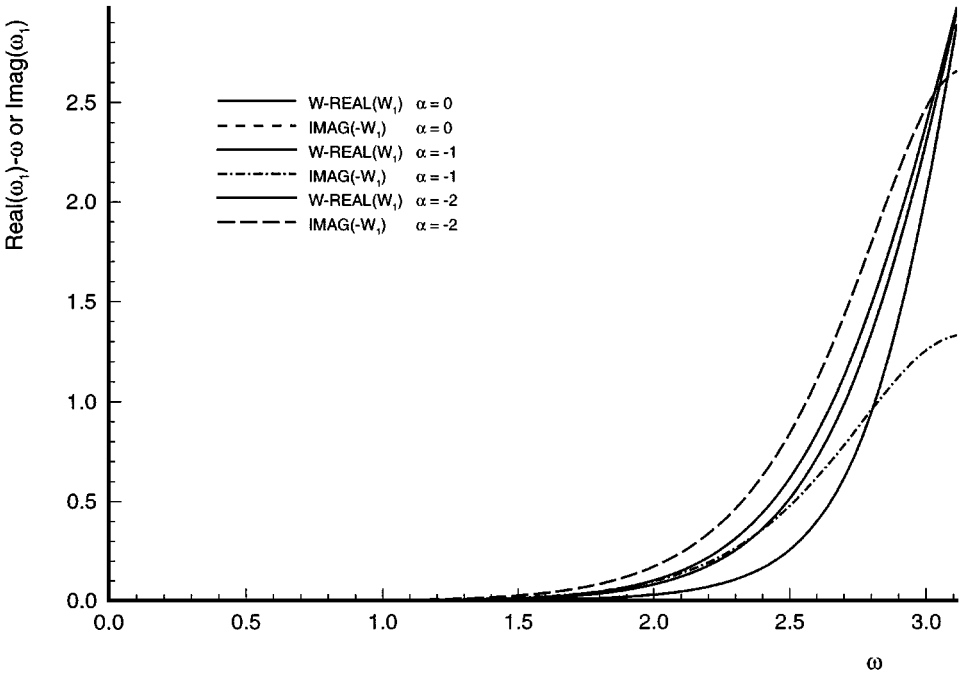

FIG. 3. Phase errors $(\Re(\omega_1) - \omega)$ and dissipation errors $\Im(\omega_1)$ of the fifth-order upwind compact schemes 5-2-3-1 with several values of α. The three solid lines from top to bottom correspond to the phase errors of the schemes using α values of 0, -1, and -2, respectively.

scheme is coupled with high-order boundary closure schemes. Therefore in addition to the dissipation condition, α should also be large enough to stabilize the inner scheme when it is coupled with boundary closure schemes. The stability analysis is based on the asymptotic stability analysis for the interior scheme with boundary closure. We do not use the stability analysis of Gustafsson *et al.* [44] based on the normal mode approach because of the complexity of the analysis for high-order upwind schemes. The asymptotic stability of the upwind schemes with numerical boundary closures is analyzed by computing the eigenvalues of the matrices obtained by spatial discretization of the wave equation. The asymptotic stability, which requires that the eigenvalues of the spatial discretization matrices contain no positive real parts, is necessary for the stability of long-time integration of the equation. The eigenvalue analysis is only a necessary condition for the stability of the schemes when the matrices do not have full sets of eigenvalues and eigenfunctions. Numerical computations show that the matrices for high-order upwind schemes with boundary conditions have full eigenvalues. For such normal matrices, the eigenvalue analysis is accurate in assessing the stability of high-order finite-difference schemes.

High-order finite-difference schemes require additional numerical boundary schemes at grid points near the boundaries of the computational domain. For a pth order interior scheme, the accuracy of boundary schemes can be $(p-1)$st order accurate without reducing the global accuracy of the interior scheme. For the fifth-order compact upwind 5-2-3-1 schemes, two numerical boundary conditions are needed on both ends of the boundaries. Fourth-order boundary schemes are used in order to maintain fifth-order overall accuracy. Both compact and explicit finite-difference schemes using one-sided bias stencils can be used as numerical boundary schemes. The fifth-order inner upwind compact schemes with fourth-order compact boundary schemes, which are represented by 4,4-5-4,4 [33], are

$$60u_0' + 180u_1' = \frac{1}{h}(-170u_0 + 90u_1 + 90u_2 - 10u_3) \tag{23}$$

$$15u_0' + 60u_1' + 15u_2' = \frac{1}{h}(-45u_0 + 45u_2) \tag{24}$$

$$b_{i-1}u_{i-1}' + b_i u_i' + b_{i+1}u_{i+1}' = \frac{1}{h}\sum_{k=-2}^{2} a_{i+k}u_{i+k} \qquad (i = 2, 3, \ldots, N-2) \tag{25}$$

$$15u_N' + 60u_{N-1}' + 15u_{N-2}' = \frac{-1}{h}(-45u_N + 45u_{N-2}) \tag{26}$$

$$60u_N' + 180u_{N-1}' = \frac{-1}{h}(-170u_N + 90u_{N-1} + 90u_{N-2} - 10u_{N-3}), \tag{27}$$

where the coefficients for the inner schemes are given by Eq. (15). Substituting the approximation above into the wave equation (10) with the non-periodic boundary condition at $x = 0$ leads to

$$\mathbf{B}\frac{dU}{dt} = \frac{c}{h}\mathbf{A}U + \mathbf{g}(t), \tag{28}$$

where $U = (u_1, \ldots, u_N)^T$, $\mathbf{g}(t) = -\frac{c}{h}u_0(t)[-10, 0, \ldots, 0, 0]^T$, and

$$\mathbf{A} = -\begin{bmatrix} -90 & 90 & 10 & & & & & \\ & & \cdot & & & & & \\ & a_{i-2} & a_{i-1} & a_i & a_{i+1} & a_{i+2} & & \\ & & & & \cdot & & & \\ & & & & & -45 & 0 & 45 \\ & & & & 10 & -90 & -90 & 170 \end{bmatrix} \tag{29}$$

$$\mathbf{B} = \begin{bmatrix} 60 & 60 & & & & & & \\ & & \cdot & & & & & \\ & & b_{i-1} & b_i & b_{i+1} & & & \\ & & & & \cdot & & & \\ & & & & & 15 & 60 & 15 \\ & & & & & & 180 & 60 \end{bmatrix}. \tag{30}$$

The asymptotic stability condition for the semi-discrete equations is that all eigenvalues of matrix $\mathbf{P} = \mathbf{B}^{-1}\mathbf{A}$ contain no positive real parts.

Figure 4 shows the eigenvalue spectra of λ_i for the upwind compact 5-2-3-1 schemes with a 4,4-5-4,4 compact boundary closure. The figure shows that sixth-order central difference compact schemes ($\alpha = 0$) are not stable when they are coupled with fourth-order boundary schemes. Carpenter *et al.* showed that for the sixth-order 5-2-3-1 central compact scheme, the stable boundary conditions are 3,4-6-4,3 schemes. However, computations

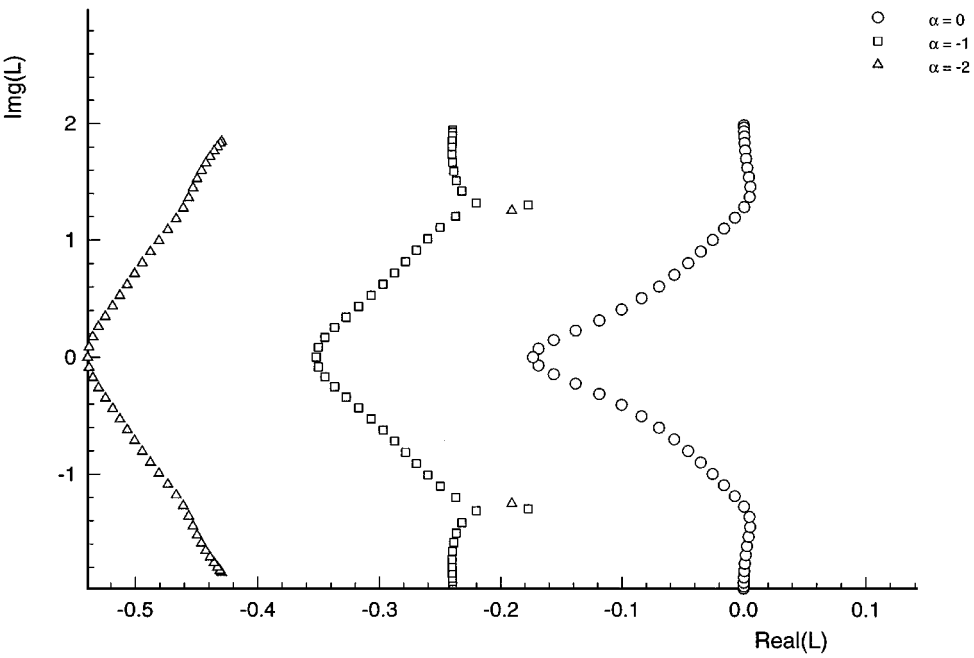

FIG. 4. Eigenvalue spectra for the fifth-order upwind compact 5-2-3-1 schemes with several values of α ($N = 50$).

using the 3,4-6-4,3 schemes are only fourth-order globally accurate even though the inner schemes are sixth-order accurate. The figure shows that the use of upwinding in inner schemes help to stabilize the schemes coupled with the high-order boundary conditions. The recommended values of the free parameter α in the upwind schemes are chosen to stabilize the high-order boundary closures. The value for α that satisfies both stability and dissipation conditions is chosen to be $\alpha = -1$, at which the scheme is stable. The fifth-order upwind compact inner scheme using the value of $\alpha = -1$ is

$$25u'_{i-1} + 60u'_i + 15u'_{i+1} = \frac{1}{h}\left(-\frac{5}{2}u_{i-2} - \frac{160}{3}u_{i-1} + 15u_i + 40u_{i+1} + \frac{5}{6}u_{i+2}\right). \quad (31)$$

In numerical simulation of Navier–Stokes equations for multi-dimensional flows, the actual value of α can be slightly different from the recommended value because of the nonlinearity of the equations.

Fifth-Order Upwind Explicit Schemes

A fifth-order explicit scheme can be obtained using a 7-3-1-0 grid stencil as

$$u'_i = \frac{1}{hb_i}\sum_{k=-3}^{3} a_{i+k}u_{i+k} - \frac{\alpha}{6!b_i}h^5\left(\frac{\partial u^6}{\partial^6 x}\right)_i + \cdots, \quad (32)$$

where

$$a_{i\pm3} = \pm 1 + \frac{1}{12}\alpha, \qquad a_{i\pm2} = \mp 9 - \frac{1}{2}\alpha$$
$$a_{i\pm1} = \pm 45 + \frac{5}{4}\alpha, \qquad a_i = -\frac{5}{3}\alpha$$
$$b_i = 60.$$

These schemes are fifth-order upwind explicit schemes when $\alpha < 0$, and they reduce to a sixth-order central scheme when $\alpha = 0$. Again, the specific value of α is determined by the conditions on dissipation errors and stability. The recommended value for α is obtained to be $\alpha = -6$, and the corresponding fifth-order upwind explicit inner scheme is

$$u'_i = \frac{1}{60h}\left(-\frac{3}{2}u_{i-3} + 12u_{i-2} - \frac{105}{2}u_{i-1} + 10u_i + \frac{75}{2}u_{i+1} - 6u_{i+2} + \frac{1}{2}u_{i+3}\right). \quad (33)$$

It is noted that the fifth-order upwind-bias (6-2-1-0) scheme of Rai and Moin [18] is a special case of the current fifth-order upwind schemes corresponding to $\alpha = -12$ and $a_{i+3} = 0$. The numerical dissipation of the current fifth-order upwind scheme given by Eq. (33) is about half as large as the upwind scheme using a upwind-bias stencil.

Figure 5 shows the dispersion and dissipation errors of the upwind explicit 7-3-1-0 schemes with three different values of α of -6, -12, -24. All seven-point explicit schemes of different values of α have the same phase errors as the sixth central scheme represented by the solid line in the figure. As $|\alpha|$ increases, the numerical dissipation increases. The figure shows that at the recommended value of $\alpha = -6$, the dissipation errors are smaller than the phase errors. The figure also includes the errors for the upwind-bias schemes [18], which correspond to $\alpha = -12$. The figure confirms that the present upwind schemes using

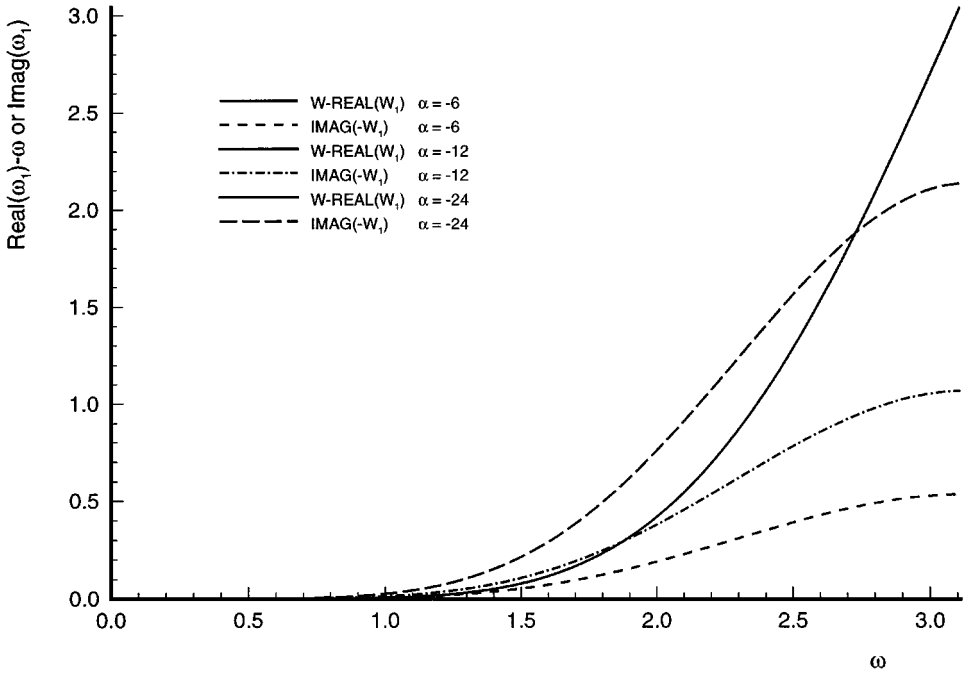

FIG. 5. Phase errors ($\Re(\omega_1) - \omega$) and dissipation errors $\Im(\omega_1)$ of the fifth-order upwind explicit schemes 7-3-1-0 with several values of α.

the recommended values of $\alpha = -6$ have smaller dissipation errors than the schemes using upwind bias stencils. Therefore, the stability and accuracy consideration in this paper leads to upwind schemes which are stable and are numerically less dissipative than a straightforward upwind scheme using an upwind-bias grid stencil.

Figure 6 shows the eigenvalue spectra for the stability of the fifth-order upwind explicit inner 7-3-1-0 schemes coupled with fourth-order explicit boundary closure schemes (4,4, 4-5-4,4,4). The figure shows that the explicit sixth-order central scheme ($\alpha = 0$) with fourth-order boundary schemes is not stable. Again, the implicit numerical dissipation in the upwind schemes has a stabilizing effect on the high-order schemes with boundary closures. At the recommended value for this scheme of $\alpha = -6$, the inner scheme with fourth-order boundary closures is stable.

Compact vs Non-compact (*Explicit*) *Schemes*

Compact schemes have been favored for the direct numerical simulations of transitional and turbulent flows because of their smaller truncation errors and narrower local grid stencils. The stability analysis in this section (Figs. 4 and 6) shows that the stability properties of compact and explicit schemes of the same order are very similar. Compared with the upwind compact schemes of the same order, high-order explicit upwind schemes can achieve the same order of accuracy with stable high-order boundary closures though more boundary closures are needed for the explicit schemes. These results suggest that the common belief that it is easier to set stable boundary conditions for compact high-order schemes because of narrower grid stencils is not true. In addition, the explicit schemes have the advantage of requiring less computations in derivative approximations and of being easier to be applied

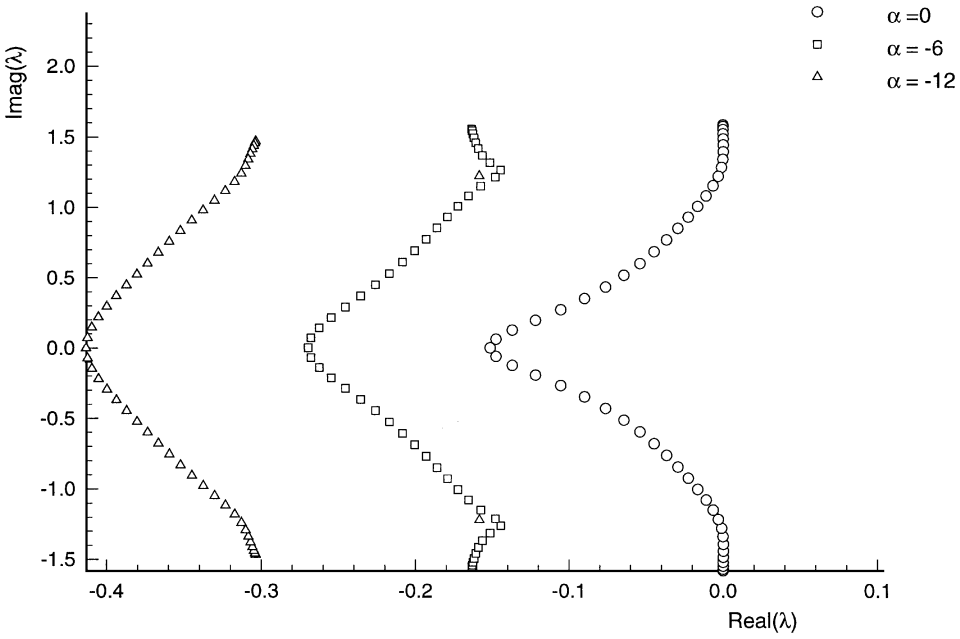

FIG. 6. Eigenvalue spectra for the fifth-order upwind explicit schemes 7-3-1-0 with several values of α ($N = 50$).

to implicit time-integration schemes for stiff systems of reactive flow equations. Therefore, both the compact and explicit schemes have their advantages and disadvantages. Between the two approaches, the compact schemes are the method of choice for discretization of derivatives in the direction with periodic boundary conditions. For discretization in the direction with non-periodic boundary conditions, the accuracy of the computations is often limited by the accuracy of boundary schemes. In this case, both explicit and compact upwind schemes can be used.

Extension to Systems of Equations

The current upwind schemes are applied to the system of equations (1) by flux splitting or by applying the schemes in each characteristic field. A simple local Lax–Friedrichs scheme can also be used to split an inviscid flux vector F_j into positive and negative wave fields so that the upwind schemes can be applied,

$$F_j = F_j^+ + F_j^-, \tag{34}$$

where

$$F_j^+ = \frac{1}{2}(F_j + \lambda U) \tag{35}$$

$$F_j^- = \frac{1}{2}(F_j - \lambda U), \tag{36}$$

where λ is a positive parameter chosen to be larger than the local maximum eigenvalues of F_j. The flux F_j^+ and F_j^- contains only positive and negative eigenvalues, respectively.

Therefore, in the spatial discretization of Eq. (1), the flux derivatives are split into two terms where the first term is discretized by an upwind high-order finite-difference method and the second term is discretized by a downwind high-order finite-difference method.

For the compressible Navier–Stokes equations (1) in a conservation-law form, the second-order derivatives do not appear explicitly in the equations. Instead, they appear as first-order derivatives in the transport flux vectors in Eq. (4). For such equations, the viscous terms can be discretized by applying central finite-difference operators for the first derivative twice [37]. The approximation of the first-order derivative for computing the viscous terms can be done using standard central compact or explicit schemes with one-sided difference approximation. For example, the sixth-order central inner schemes (5-3-3-1) and the sixth-order compact boundary schemes are

$$60u'_0 + 300u'_1 = \frac{1}{h}(-197u_0 - 25u_1 + 300u_2 - 100u_3 + 25u_4 - 3u_5) \quad (37)$$

$$\frac{15}{2}u'_0 + 60u'_1 + 45u'_2 = \frac{1}{h}\left(-\frac{215}{8}u_0 - 50u_1 + \frac{135}{2}u_2 + 10u_3 - \frac{5}{8}u_4\right) \quad (38)$$

$$b_{i-1}u'_{i-1} + b_i u'_i + b_{i+1}u'_{i+1} = \frac{1}{h}\sum_{k=-2}^{2} a_{i+k}u_{i+k} \qquad (i = 2, 3, \ldots, N-2) \quad (39)$$

$$45u'_{N-2} + 60u'_{N-1} + \frac{15}{2}u'_N = \frac{1}{h}\left(\frac{215}{8}u_N + 50u_{N-1} - \frac{135}{2}u_{N-2} - 10u_{N-3} + \frac{5}{8}u_{N-4}\right) \quad (40)$$

$$60u'_N + 300u'_{N-2} = \frac{1}{h}(197u_N + 25u_{N-1} - 300u_{N-2} + 100u_{N-3} - 25u_{N-4} + 3u_{N-5}), \quad (41)$$

where the coefficients for the inner schemes are given by Eq. (15) with $\alpha = 0$. The formulas can be written into matrix form

$$\mathbf{B}U' = \mathbf{A}U, \quad (42)$$

where $U = (u_0, \ldots, u_N)^T$. The second-order derivative in viscous terms is obtained by applying the first-order operator twice, i.e.,

$$\mathbf{B}U'' = \mathbf{A}U' = \mathbf{A}\mathbf{B}^{-1}\mathbf{A}U. \quad (43)$$

Another approach is to apply high-order central schemes directly to second-order derivatives in the equations. While the previous approach is easier to be implemented in simulations, the direct discretization of the second-order derivatives is more stable in practical calculations of the Navier–Stokes equations. The previous approach also leads to a wider grid stencil than applying central compact schemes directly to a second-order derivative directly.

Effect of Grid Stretching

The high-order schemes in this paper are derived for uniform grids. For viscous flow simulations, however, grids are often strongly stretched in the direction normal to the wall in order to cluster more grid points near the wall. We investigate the effect of grid stretching

on the stability and accuracy of high-order difference schemes applied to a linear wave equation. Two approaches can be used to apply a high-order finite-difference scheme to the wave equation in a stretched grid. The first approach transforms the equation in the physical domain of a stretched grid into the computational domain of a uniform grid by a coordinate transformation. The transformed equation is then discretized by the finite-difference scheme in the uniform computational grid. The second approach applies the high-order polynomial interpolation directly to the stretched physical grid without using the coordinate transformation. The asymptotic stability properties, and phase and dissipation errors, of the finite-difference scheme in the stretched grid can be investigated using the same analyses of the preceding sections for the uniform grids.

The asymptotic stability analysis for the two approaches is carried out for the fifth-order upwind explicit 7-3-1-0 scheme with $\alpha = -12$ coupled with the fourth-order explicit boundary closure schemes (4,4,4-5-4,4,4). The specific stretched grid is specified by the following coordinate transformation [45],

$$\xi = \alpha - (1-\alpha)\frac{\ln((\beta + x(2\alpha+1) - 2\alpha)/(\beta - x(2\alpha+1) + 2\alpha))}{\ln((\beta+1)/(\beta-1))} \qquad (0 \le x \le 1, 0 \le \xi \le 1), \quad (44)$$

where a uniform grid ξ in the computational domain is transformed into a stretched grid x in the physical domain, and the extent of the stretching is determined by the values of α and β. The values used in the analysis are $\alpha = 0.5$ and $\beta = 1.01015$. Figure 7 shows the

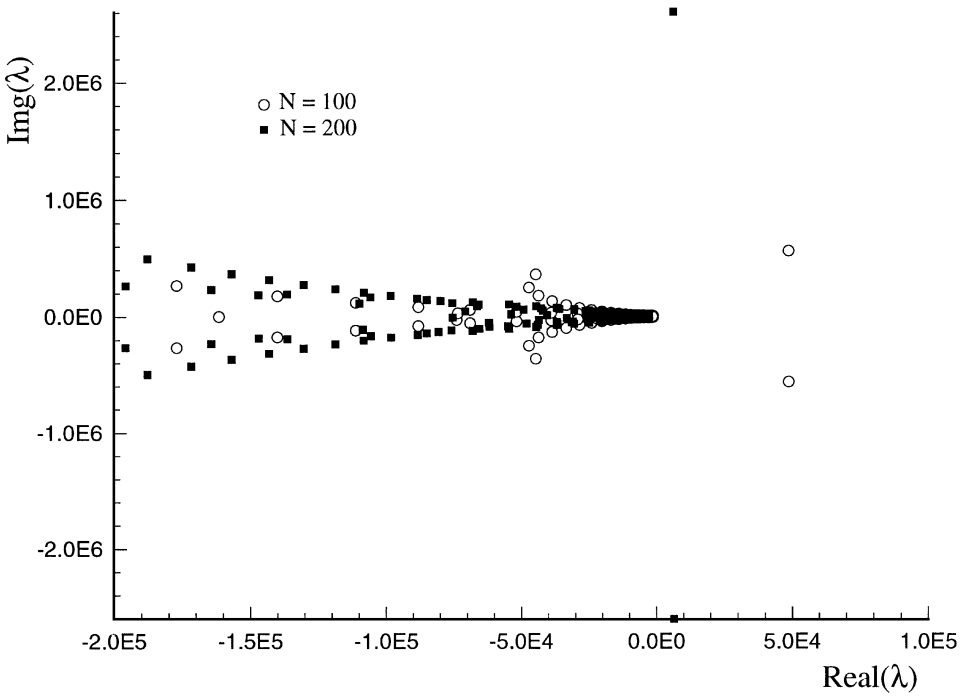

FIG. 7. Eigenvalue spectrum for the fifth-order upwind explicit scheme (7-3-1-0 and $\alpha = -12$) applied to the linear wave equation by using the approach of coordinate transformation in two sets of stretched grids ($N = 100, 200$).

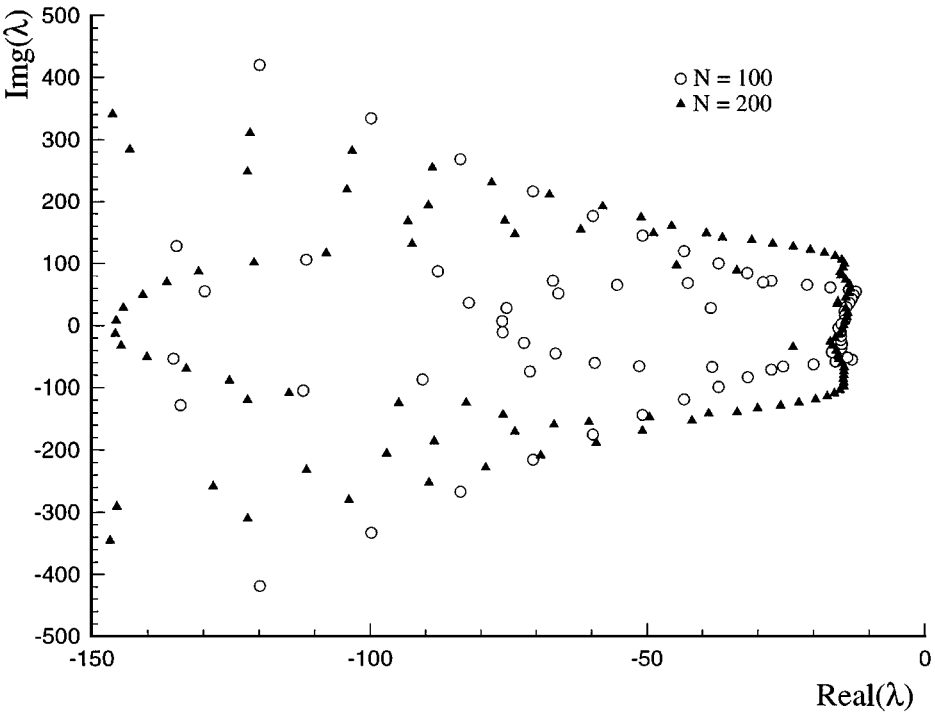

FIG. 8. Eigenvalue spectrum for the fifth-order upwind explicit scheme (7-3-1-0 and $\alpha = -12$) applied to the linear wave equation by using the approach of direct polynomial interpolation in the non-uniform physical coordinates in two sets of stretched grids ($N = 100, 200$).

eigenvalue spectrum for the fifth-order scheme applied to the wave equation by using the approach of coordinate transformation. The figure shows that the scheme becomes unstable for strongly stretched grids. As the number of grid points increases, the relative stretching of the grid reduces and the scheme becomes less unstable. Further calculations also show that the scheme eventually becomes stable when the grid is uniform enough. Therefore, grid stretching has a destabilizing effect when the fifth-order scheme is applied to the wave equation by a coordinate transformation. On the other hand, if the high-order scheme is obtained by a direct high-order polynomial interpolation in the physical non-uniform grid, the asymptotic stability analysis shows that such a high-order scheme is stable for highly stretched grids as shown by Fig. 8. Similar asymptotic stability analysis has also been carried out for a linear one-dimensional heat equation. It is found that the grid stretching does not have destabilizing effects on the stability of the diffusive equation calculation using high-order central schemes based on coordinate transformation. Therefore, the new high-order schemes based on the approach of coordinate transformation will be stable for a stretched grid in the boundary layers where the equations are dominated by viscous terms. On the other hand, for flow fields with strong convection, such as the flow immediately behind the bow shocks, the grid stretching near the shocks may cause numerical instability if high-order schemes are applied in transformed coordinates. In such cases, the high-order schemes should be applied directly in the physical coordinates.

The effect of grid stretching on the accuracy of the high-order schemes is investigated by computing the dispersion and dissipation errors using similar formulas as Eqs. (20) and (21). Figure 9 shows the dispersion and dissipation errors of the fifth-order upwind explicit

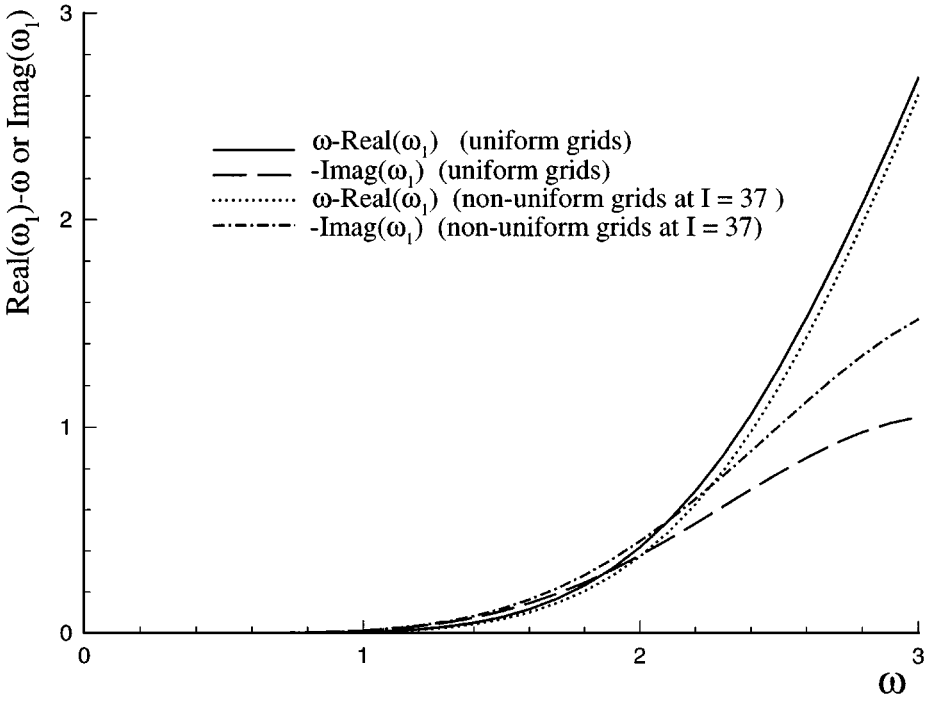

FIG. 9. Phase errors $(\Re(\omega_1) - \omega)$ and dissipation errors $\Im(\omega_1)$ of the fifth-order upwind explicit scheme (7-3-1-0 and $\alpha = -12$) applied to the linear wave equation by using the approach of direct polynomial interpolation in the non-uniform physical coordinates in a set of $N = 120$ stretched grids.

7-3-1-0 schemes with $\alpha = -12$ in the same stretched grid used in the stability analysis. The accuracy of the scheme in the stretched grid is compared with that in a uniform grid of the same size. The figure shows that the dissipation and the phase errors in a stretched grid are comparable or slightly larger to those in the uniform grid.

4. HIGH-ORDER SHOCK-FITTING FORMULATIONS

A shock-fitting method is used to compute unsteady three-dimensional viscous hypersonic flow over blunt bodies. The governing equations are solved in general curvilinear three-dimensional coordinates (ξ, η, ζ, τ) along body fitted grid lines shown in Fig. 10. The bow shock is treated as a computational boundary where the transient shock movement is solved as a part of the solutions. Consequently, the grid surface of $\eta =$ constant is unsteady due to the shock movement, but the grid surfaces of $\xi =$ constant and $\zeta =$ constant are fixed planar surfaces during the calculations. Therefore, the transformation relations between the Cartesian coordinates and the (ξ, η, ζ, τ) coordinates for the current shock-fitting computations are

$$\begin{cases} \xi = \xi(x, y, z) \\ \eta = \eta(x, y, z, t) \\ \zeta = \zeta(x, y, z) \\ \tau = t \end{cases} \Leftrightarrow \begin{cases} x = x(\xi, \eta, \zeta, \tau) \\ y = y(\xi, \eta, \zeta, \tau) \\ z = z(\xi, \eta, \zeta, \tau) \\ t = \tau, \end{cases} \tag{45}$$

where $\xi_t = 0$ and $\zeta_t = 0$.

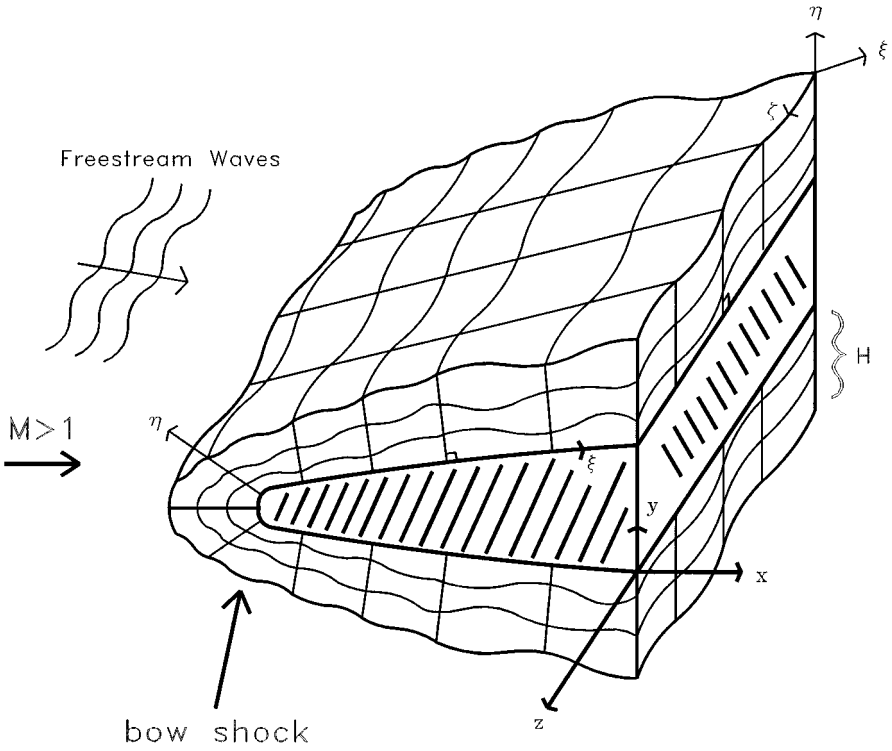

FIG. 10. A schematic of three-dimensional shock-fitting grids for the direct numerical simulation of hypersonic boundary-layer receptivity to freestream disturbances over a blunt leading edge.

The governing equation (1) is transformed into the computational domain (ξ, η, ζ, τ) as

$$\frac{1}{J}\frac{\partial U}{\partial \tau} + \frac{\partial E'}{\partial \xi} + \frac{\partial F'}{\partial \eta} + \frac{\partial G'}{\partial \zeta} + \frac{\partial E'_v}{\partial \xi} + \frac{\partial F'_v}{\partial \eta} + \frac{\partial G'_v}{\partial \zeta} + U\frac{\partial (1/J)}{\partial \tau} = \frac{W}{J}, \tag{46}$$

where

$$E' = \frac{F_1\xi_x + F_2\xi_y + F_3\xi_z}{J} \tag{47}$$

$$F' = \frac{F_1\eta_x + F_2\eta_y + F_3\eta_z + U\eta_t}{J} \tag{48}$$

$$G' = \frac{F_1\zeta_x + F_2\zeta_y + F_3\zeta_z}{J} \tag{49}$$

$$E'_v = \frac{F_{v1}\xi_x + F_{v2}\xi_y + F_{v3}\xi_z}{J} \tag{50}$$

$$F'_v = \frac{F_{v1}\eta_x + F_{v2}\eta_y + F_{v3}\eta_z}{J} \tag{51}$$

$$G'_v = \frac{F_{v1}\zeta_x + F_{v2}\zeta_y + F_{v3}\zeta_z}{J}, \tag{52}$$

where J is the Jacobian of the coordinate transformation, and ξ_x, ξ_y, ξ_z, η_x, η_y, η_z, η_t, ζ_x, ζ_y, and ζ_z are the grid transformation metrics which are functions of the distance $H(\xi, \zeta, \tau)$ between the shock and the wall along a $\eta =$ constant grid line, and the time derivative H_τ.

In Eq. (46), the transformed inviscid fluxes E', F', and G' are standard flux terms with full sets of eigenvalues and eigenvectors. The transport flux terms E'_v, F'_v, and G'_v contain first-order spatial derivatives of velocity and temperature. The governing equations (46) are discretized in the uniform computational space.

The shock-fitting method treats the bow shock as a computational boundary at

$$\eta(x, y, z, t) = \eta_{\max} = \text{constant}. \tag{53}$$

The flow variables immediately behind the shock are determined by the Rankine–Hugoniot relation across the shock and a characteristic compatibility equation from the flow field behind the shock. The position and velocity of the shock front are functions of $H(\xi, \zeta, \tau)$ and $H_\tau(\xi, \zeta, \tau)$, which are solved as independent flow variables using high-order finite-difference methods. The normal vector of the shock front is

$$\mathbf{n} = \frac{\eta_x \mathbf{i} + \eta_y \mathbf{j} + \eta_z \mathbf{k}}{|\nabla \eta|} \tag{54}$$

and the velocity of the shock front in the direction of $\mathbf{n}$ is

$$v_n = -\frac{\eta_t}{|\nabla \eta|}, \tag{55}$$

where $|\nabla \eta| = \sqrt{\eta_x^2 + \eta_y^2 + \eta_z^2}$.

The flow variables across the shock are governed by the Rankine–Hugoniot conditions,

$$F'_s = F'_0 \tag{56}$$

where the subscript s represents the variable immediately behind the shock and subscript 0 represents the variable on the free stream side of the shock surface. The flux F' is the flux in the computational space along the η grids line. Equation (48) leads to

$$F' = \frac{|\nabla \eta|}{J}(\mathbf{F} \cdot \mathbf{n} - v_n U), \tag{57}$$

where $\mathbf{F} = F_1 \mathbf{i} + F_2 \mathbf{j} + F_3 \mathbf{k}$.

The Rankine–Hugoniot relations (56) lead to jump conditions for flow variables behind the shock as functions of U_0 and the grid velocity v_n, i.e.,

$$p_s = p_0 \left[1 + \frac{2\gamma}{\gamma + 1}\left(M_{n0}^2 - 1\right)\right] \tag{58}$$

$$\rho_s = \rho_0 \left[1 + \frac{(\gamma + 1) M_{n0}^2}{(\gamma - 1) M_{n0}^2 + 2}\right] \tag{59}$$

$$u_{ns} = v_n + \frac{\rho_0}{\rho_s}(u_{n0} - v_n) \tag{60}$$

$$\mathbf{u}_{ts} = \mathbf{u}_{t0} = \mathbf{u}_0 - u_{n0}\mathbf{n} \tag{61}$$

$$\mathbf{u}_s = \mathbf{u}_{ts} + u_{ns}\mathbf{n} = \mathbf{u}_0 + (u_{ns} - u_{n0})\mathbf{n}, \tag{62}$$

where M_{n0} is the normal component of the freestream Mach number relative to the shock motions, $\mathbf{u}$ is the velocity vector, $\mathbf{u}_t$ is the tangential velocity vector, and u_n is the normal

velocity component. In order to compute the flow variable behind the shock using the shock jump conditions above, the velocity of the shock front v_n is needed. The shock normal velocity is determined by a characteristic compatibility equation at the grid point immediately behind the shock.

The shock-fitting computations and the shock geometry transformation relations are greatly simplified if the characteristic compatibility equation is written in the conservation-law form, which can be derived directly from Eq. (46) in the direction along the η coordinates. Specifically, the interior equation (46) in the computational domain at the point immediately behind the shock front can be written as

$$\frac{1}{J}\frac{\partial U}{\partial \tau}+\frac{\partial F'}{\partial \eta}=\frac{W}{J}-\frac{\partial E'}{\partial \xi}-\frac{\partial G'}{\partial \zeta}-\frac{\partial E'_v}{\partial \xi}-\frac{\partial F'_v}{\partial \eta}-\frac{\partial G'_v}{\partial \zeta}-U\frac{\partial (1/J)}{\partial \tau}, \tag{63}$$

where the equation is evaluated at point s immediately behind the shock. In the equations, the Jacobian matrix, $B'_s=(\partial F'/\partial U)_s$, has the eigenvalues

$$\frac{|\nabla\eta|}{J}(u_n-v_n)_s,\ldots,\frac{|\nabla\eta|}{J}(u_n-v_n)_s,\frac{|\nabla\eta|}{J}(u_n-v_n-c)_s,\frac{|\nabla\eta|}{J}(u_n-v_n+c)_s \tag{64}$$

where c is speed of the sound. The corresponding left eigenvectors are

$$\mathbf{l_1},\mathbf{l_2},\ldots,\mathbf{l_{N-1}},\mathbf{l_N}, \tag{65}$$

where N is the number of independent variables in the equations, and

$$\mathbf{l_N}=\frac{1}{c^2}\begin{bmatrix}\frac{\gamma-1}{2}\mathbf{u}\cdot\mathbf{u}-cu_n\\ -\left(\frac{1}{2}cn_x-\frac{\gamma-1}{2}u\right)\\ -\left(\frac{1}{2}cn_y-\frac{\gamma-1}{2}v\right)\\ -\left(\frac{1}{2}cn_z-\frac{\gamma-1}{2}w\right)\\ \frac{\gamma-1}{2}\end{bmatrix}_s. \tag{66}$$

The left eigenvector behind the shock satisfies

$$\mathbf{l_N}\cdot B'_s=\frac{|\nabla\eta|}{J}(u_n-v_n+c)_s\mathbf{l_N}. \tag{67}$$

The characteristic field approaching the shock from behind corresponds to the eigenvalue with a positive sign which is $\frac{|\nabla\eta|}{J}(u_n-v_n+c)_s$. The corresponding eigenvector is $\mathbf{l_N}$. The compatibility relation at a grid point immediately behind the shock for this characteristic field can be obtained by multiplying Eq. (63) by $\mathbf{l_N}$,

$$\mathbf{l_N}\cdot\left(\frac{\partial U}{\partial \tau}\right)=\mathbf{l_N}\cdot\left(\frac{W}{J}-\frac{\partial E'}{\partial \xi}-\frac{\partial F'}{\partial \eta}-\frac{\partial G'}{\partial \zeta}-\frac{\partial E'_v}{\partial \xi}-\frac{\partial F'_v}{\partial \eta}-\frac{\partial G'_v}{\partial \zeta}-U\frac{\partial (1/J)}{\partial \tau}\right)J. \tag{68}$$

On the other hand, the shock jump condition (56) can be rewritten as

$$[F']=(\mathbf{F_s}-\mathbf{F_0})\cdot\mathbf{a}+(U_s-U_0)b=0, \tag{69}$$

where

$$\mathbf{a} = \left(\frac{\eta_x}{J}\right)_s \mathbf{i} + \left(\frac{\eta_y}{J}\right)_s \mathbf{j} + \left(\frac{\eta_z}{J}\right)_s \mathbf{k} \tag{70}$$

$$b = \left(\frac{\eta_t}{J}\right)_s. \tag{71}$$

Taking the derivative of Eq. (69) with respective to τ in the computational space leads to

$$B_s' \frac{\partial U_s}{\partial \tau} - B_0' \frac{\partial U_0}{\partial \tau} + (\mathbf{F_s} - \mathbf{F_0}) \cdot \frac{\partial \mathbf{a}}{\partial \tau} + (U_s - U_0) \frac{\partial b}{\partial \tau} = 0, \tag{72}$$

where the flux Jacobian

$$B' = \frac{\partial F'}{\partial U} \tag{73}$$

is the Jacobian of the η direction flux defined in the conservation equations (46), and

$$\frac{\partial \mathbf{a}}{\partial \tau} = \frac{\partial (\eta_x/J)_s}{\partial \tau}\mathbf{i} + \frac{\partial (\eta_y/J)_s}{\partial \tau}\mathbf{j} + \frac{\partial (\eta_z/J)_s}{\partial \tau}\mathbf{k} \tag{74}$$

$$\frac{\partial b}{\partial \tau} = \frac{\partial (\eta_\tau/J)_s}{\partial \tau}. \tag{75}$$

These time derivatives of the grid metrics can be derived by the same methods as those used in discretization of the interior equations.

Finally, the equation for the shock velocity can be obtained by multiplying both sides of Eq. (72) by $\mathbf{l_N}$ and using the relation of (67), i.e.,

$$\frac{\partial b}{\partial \tau} = \frac{-1}{[\mathbf{l_N} \cdot (U_s - U_0)]} \tag{76}$$

$$\left[\frac{|\nabla \eta|}{J}(u_n - v_n + c)_s \mathbf{l_N} \cdot \left(\frac{\partial U}{\partial \tau}\right)_s + \mathbf{l_N} \cdot (\mathbf{F_s} - \mathbf{F_0}) \cdot \frac{\partial \mathbf{a}}{\partial \tau} - (\mathbf{l_N} \cdot \mathbf{B_0'}) \frac{\partial U_0}{\partial \tau}\right], \tag{77}$$

where the term $\mathbf{l_N} \cdot \frac{\partial U_s}{\partial \tau}$ is computed using the characteristic relation (68), in which the spatial derivatives are discretized together with the discretization of the interior points for the Eq. (46) using the same schemes at the interior algorithm applied to boundary behind the shock. In the equation above, $\frac{\partial b}{\partial \tau}$ and $\frac{\partial \mathbf{a}}{\partial \tau}$ can be expressed as a function of H and H_τ as

$$\frac{\partial b}{\partial \tau} = d_1(\xi, \zeta, H, H_\tau) + d_2(\xi, \zeta, H, H_\tau) \frac{\partial H_\tau}{\partial \tau} \tag{78}$$

$$\frac{\partial \mathbf{a}}{\partial \tau} = \mathbf{g}(\xi, \zeta, H, H_\tau), \tag{79}$$

where $H = H(\xi, \zeta, \tau)$ is the distance between the shock and the wall along an $\eta =$ constant grid line, and $H_\tau = \partial H/\partial \tau$. The coefficients, d_1, d_2, and vector $\mathbf{g}$ are functions of grid metrics.

Therefore, the governing equations for the two independent variables, H and H_τ, for shock motions can be obtained from Eqs. (77) to (79) in the form

$$\begin{cases} \frac{\partial H_\tau}{\partial \tau} = f\left(\xi, \zeta, U_s, \mathbf{l_N} \cdot \left(\frac{\partial U}{\partial \tau}\right)_s, U_0, \frac{\partial U_0}{\partial \tau}, H, H_\tau\right) \\ \frac{\partial H}{\partial \tau} = H_\tau. \end{cases} \tag{80}$$

The two equations are additional governing equations for the shock normal velocity and shock shape. They are integrated in time simultaneously with the interior flow variables

and are advanced in time using the same Runge–Kutta methods as the interior Eq. (46). After the values of H and H_τ are determined, the flow variables behind the shock can be computed by the jump conditions across the shock using Eqs. (58) to (62). The grids and metrics are modified according to the new values of H and H_τ.

The current formulation is simple in high-order implementation because the governing equations for the shock movement are derived using conservative variable and flux Jacobian in Eq. (72) using the relation (67). The same discretization of the interior governing equations is used to evaluate $(\frac{\partial U_s}{\partial \tau})_s$ at grid points immediately behind the shock. In addition, all geometric definitions of the shock front are the same as the grid metrics used in the interior equation transformation, which are stored in the computer. In doing so, the current approach avoids the complication of using the non-conservation variables and locally defined geometric parameters for the shock front in deriving the time derivatives of the shock jump condition.

5. SEMI-IMPLICIT RUNGE–KUTTA SCHEMES

The spatial discretization of the governing equations leads to a system of first-order ordinary differential equations for the flow variables. Explicit Runge–Kutta schemes of up to third order accuracy, such as the low-storage Runge–Kutta schemes of Williamson [42], can be used to advance the equations in time for the DNS of non-reacting hypersonic flows. For reacting hypersonic flow simulations, the thermo-chemical source term $W(U)$ is often stiff in temporal discretization. Semi-implicit Runge–Kutta schemes of up to third order derived by Zhong [30] can be used. The semi-implicit Runge–Kutta schemes are briefly described below. The details of the derivations of the third-order semi-implicit Runge–Kutta schemes can be found in [30].

The spatial discretization of reacting flow equations leads to

$$\frac{d\mathbf{u}}{dt} = \mathbf{f}(\mathbf{u}) + \mathbf{g}(\mathbf{u}), \tag{81}$$

where $\mathbf{u}$ is the vector of discretized flow field variables, $\mathbf{f}$ contains the non-stiff terms resulting from spatial discretization of the flux terms which can be computed explicitly, and $\mathbf{g}$ contains the stiff thermo-chemical source terms which need to be computed implicitly. For high-order temporal integration of the stiff governing equations, Ref. [30] derived three versions of 3-stage third-order semi-implicit Runge–Kutta schemes for integrating Eq. (81) by simultaneously treating $\mathbf{f}$ explicitly and $\mathbf{g}$ implicitly. The coefficients of the semi-implicit schemes were derived such that the schemes are high-order accurate with the simultaneous coupling between the implicit and explicit terms. In addition, the schemes are unconditionally stable for the stiff terms when a CFL condition is satisfied for the explicit terms.

ASIRK-3A Scheme

$$\begin{cases} \mathbf{k}_1 = h\{\mathbf{f}(\mathbf{u}^n) + \mathbf{g}(\mathbf{u}^n + a_1\mathbf{k}_1)\} \\ \mathbf{k}_2 = h\{\mathbf{f}(\mathbf{u}^n + b_{21}\mathbf{k}_1) + \mathbf{g}(\mathbf{u}^n + c_{21}\mathbf{k}_1 + a_2\mathbf{k}_2)\} \\ \mathbf{k}_3 = h\{\mathbf{f}(\mathbf{u}^n + b_{31}\mathbf{k}_1 + b_{32}\mathbf{k}_2) + \mathbf{g}(\mathbf{u}^n + c_{31}\mathbf{k}_1 + c_{31}\mathbf{k}_2 + a_3\mathbf{k}_3)\} \\ \mathbf{u}^{n+1} = \mathbf{u}^n + \omega_1\mathbf{k}_1 + \omega_2\mathbf{k}_2 + \omega_3\mathbf{k}_3 \end{cases}$$

ASIRK-3B Scheme

$$\begin{cases} \big[\mathbf{I} - ha_1\mathbf{J}(\mathbf{u}^n)\big]\mathbf{k}_1 = h\{\mathbf{f}(\mathbf{u}^n) + \mathbf{g}(\mathbf{u}^n)\} \\ \big[\mathbf{I} - ha_2\mathbf{J}(\mathbf{u}^n)\big]\mathbf{k}_2 = h\big\{\mathbf{f}\big(\mathbf{u}^n + b_{21}\mathbf{k}_1\big) + \mathbf{g}\big(\mathbf{u}^n + c_{21}\mathbf{k}_1\big)\big\} \\ \big[\mathbf{I} - ha_3\mathbf{J}(\mathbf{u}^n)\big]\mathbf{k}_3 = h\big\{\mathbf{f}\big(\mathbf{u}^n + b_{31}\mathbf{k}_1 + b_{32}\mathbf{k}_2\big) + \mathbf{g}\big(\mathbf{u}^n + c_{31}\mathbf{k}_1 + c_{32}\mathbf{k}_2\big)\big\} \\ \mathbf{u}^{n+1} = \mathbf{u}^n + \omega_1\mathbf{k}_1 + \omega_2\mathbf{k}_2 + \omega_3\mathbf{k}_3 \end{cases}$$

ASIRK-3C Scheme

$$\begin{cases} \big[\mathbf{I} - ha_1\mathbf{J}(\mathbf{u}^n)\big]\mathbf{k}_1 = h\{\mathbf{f}(\mathbf{u}^n) + \mathbf{g}(\mathbf{u}^n)\} \\ \big[\mathbf{I} - ha_2\mathbf{J}\big(\mathbf{u}^n + c_{21}\mathbf{k}_1\big)\big]\mathbf{k}_2 = h\big\{\mathbf{f}\big(\mathbf{u}^n + b_{21}\mathbf{k}_1\big) + \mathbf{g}\big(\mathbf{u}^n + c_{21}\mathbf{k}_1\big)\big\} \\ \big[\mathbf{I} - ha_3\mathbf{J}\big(\mathbf{u}^n + c_{31}\mathbf{k}_1 + c_{32}\mathbf{k}_2\big)\big]\mathbf{k}_3 = h\big\{\mathbf{f}\big(\mathbf{u}^n + b_{31}\mathbf{k}_1 + b_{32}\mathbf{k}_2\big) \\ \qquad\qquad + \mathbf{g}\big(\mathbf{u}^n + c_{31}\mathbf{k}_1 + c_{32}\mathbf{k}_2\big)\big\} \\ \mathbf{u}^{n+1} = \mathbf{u}^n + \omega_1\mathbf{k}_1 + \omega_2\mathbf{k}_2 + \omega_3\mathbf{k}_3, \end{cases}$$

where $\mathbf{J}$ is the Jacobian of $\mathbf{g}$ vector. The parameters are

ASIRK-3A, ASIRK-3B, and ASIRK-3C

$$\begin{array}{lll} \omega_1 = \frac{1}{8} & \omega_2 = \frac{1}{8} & \omega_3 = \frac{3}{4} \\ b_{21} = \frac{8}{7} & b_{31} = \frac{71}{252} & b_{32} = \frac{7}{36} \end{array}$$

ASIRK-3A

$$\begin{array}{lll} a_1 = .485561 & a_2 = .951130 & a_3 = .189208 \\ c_{21} = .306727 & c_{31} = .45 & c_{32} = -.263111 \end{array}$$

ASIRK-3B

$$\begin{array}{lll} a_1 = 1.40316 & a_2 = .322295 & a_3 = .315342 \\ c_{21} = 1.56056 & c_{31} = \frac{1}{2} & c_{32} = -.696345 \end{array}$$

ASIRK-3C

$$\begin{array}{lll} a_1 = .797097 & a_2 = .591381 & a_3 = .134705 \\ c_{21} = 1.05893 & c_{31} = \frac{1}{2} & c_{32} = -.375939, \end{array}$$

where a_1, a_2, a_3, c_{21}, and c_{32} are irrational numbers with six significant digits. The double-precision values of these parameters can be found in [30]. The first method above uses diagonally implicit Runge–Kutta methods for the stiff term $\mathbf{g}$, which leads to a nonlinear equation at every stage of the implicit calculations if $\mathbf{g}$ is a nonlinear function of $\mathbf{u}$. The second and third methods use linearized implicit schemes for the stiff term $\mathbf{g}$. Methods B and C, which are similar to linearized implicit methods commonly used in computing reactive flows, are more efficient than the full implicit method A. However, for some stiff nonlinear problems, method A is necessary because it is more stable than the Rosenbrock semi-implicit Runge–Kutta method.

6. RESULTS OF NUMERICAL EXPERIMENTS

The new high-order upwind schemes with and without the shock-fitting procedure are validated and tested in computations for the linear wave equation and nonlinear Navier–Stokes equations. The numerical accuracy and stability of the high-order upwind schemes without the shock-fitting procedure are first validated in computations of the linear model wave equation. The schemes are then applied to the computations of the Navier–Stokes equations for steady and unsteady supersonic Couette flows, where the shock fitting procedure is not needed. The numerical solutions are compared with analytical solutions and are evaluated by grid refinements. The upwind schemes with the shock-fitting procedure are subsequently applied to a two-dimensional steady hypersonic flow over a cylinder. The numerical results are compared with experimental results and evaluated by grid refinements. The focus of the test cases is on the high-order upwind schemes and the shock-fitting formulations. Therefore, the Navier–Stokes equations with perfect-gas assumption are assumed in the test cases of this paper. The applications of semi-implicit Runge–Kutta schemes for reacting hypersonic flow simulations are an independent research topic of their own. They are presented in other papers [46].

Linear 1-D Wave Equation

The new compact and explicit upwind schemes are tested in computations for the one-dimensional linear wave equation (10). Both periodic and non-periodic boundary conditions are computed to test the accuracy of schemes with and without boundary closures. The parameters of the calculations are $a = 0, b = 1, c = 1$, $N + 1$ uniform grid points, and the initial condition is

$$u(x, 0) = \sin(\omega\pi x), \qquad 0 \le x \le 1. \tag{82}$$

The temporal time marching scheme is a third-order explicit Runge–Kutta scheme. In order to compare spatial discretization errors of different schemes, a small CFL number of 0.005 is used so that the temporal discretization errors are negligible compared with those of the spatial discretization. Grid refinements in time are used to ensure that the solutions are independent of the time step sizes.

The results of the new upwind schemes are compared with those of the sixth-order standard central compact scheme with stable 3,4-6-4,3 boundary closure and a fourth-order compact central 7-3-5-2 scheme of Lele [32] for spectral-like resolution. The 7-3-5-2 optimized scheme [32] is fourth-order accurate but has smaller phase errors at large wave number ω. Though the order of the scheme is lower than the maximum achievable order for the stencil it used, the degree of freedom in deriving the coefficients is used to minimize the phase errors in resolving high wave-number modes. Compared with schemes with maximum order accuracy, the optimized schemes have lower accuracy for resolving modes of small ω, but they have higher accuracy in resolving modes of larger ω. It is expected that the optimized schemes resolve a range of length scales better than the maximum order schemes. Similar approaches have also been used in optimizing finite-difference schemes for various applications [36, 38, 47, 48]. The optimized schemes, however, are derived without considering the effects of boundary conditions. For computations with non-periodic boundary conditions, it is not clear how boundary closure schemes would affect the performance of the optimized schemes.

TABLE I
L^1 Errors of Solving Wave Equation with Periodic Boundary Conditions

		L^1 errors of three schemes		
ω	$L/\Delta x$	9-4-1-0 ($\alpha = 36$)	7-3-3-1 ($\alpha = 36$)	7-3-5-2 (Lele)
2	50.0	0.18 (−7)	0.11 (−7)	0.44 (−5)
4	25.0	0.49 (−5)	0.26 (−5)	0.17 (−3)
6	16.7	0.13 (−3)	0.66 (−4)	0.10 (−2)
8	12.5	0.14 (−2)	0.66 (−3)	0.41 (−2)
10	10.0	0.93 (−2)	0.39 (−2)	0.12 (−1)
12	8.3	0.41 (−1)	0.16 (−1)	0.28 (−1)
14	7.1	0.14	0.54 (−1)	0.55 (−1)
16	6.3	0.38	0.15	0.95 (−1)
18	5.6	0.73	0.31	0.15
20	5.0	0.72	0.51	0.21

Note. The results correspond to test cases of different values of ω with a fixed number of grids $N = 50$ in a fixed computational domain (0, 1). $L/\Delta x$ is the number of grids used to resolve one wave period in space.

A. Periodic boundary conditions. The upwind and central schemes with periodic boundary conditions are tested in computing the wave equation in a fixed computational domain (0, 1) using a fixed number of uniform grids $N = 50$. For each inner scheme, twenty runs are made using different values of wave number ω so that the effects of grid resolution on the numerical errors of the scheme can be examined. The number of grid points used to span a single wave length in space is $L/\Delta x$, where the wave length is $L = 2\pi/\omega$. The solutions are advanced in time in more than 10 periods for long time integration. Three schemes are used in spatial discretizations: (1) current seventh-order upwind explicit scheme 9-4-1-0 with $\alpha = 36$, (2) current seventh-order upwind compact scheme 7-3-3-1 with $\alpha = 36$, and (3) fourth-order spectral-like upwind compact schemes 7-3-5-2.

Table I shows the L^1 errors of the numerical solutions using the three schemes for 20 runs of different ω. As ω increases, the number of wave modes in the domain increases and there are less grid points in resolving each wave mode. The results show that the compact 7-3-3-1 scheme is more accurate than the explicit 9-4-1-0 for the current periodic problem. The upwind schemes 9-4-1-0 and 7-3-3-1, which have higher order formal accuracy, are more accurate than the spectral-like 7-3-5-2 scheme for smaller ω. But as ω increases and there are less grid points in resolving the waves, the spectral-like scheme becomes more accurate. Therefore, for the wave equation with periodic boundary conditions, the spectral-like compact schemes with reduced formal order of accuracy have better overall resolution than standard high-order schemes in resolving a wide range of wave modes. These results are expected because the optimized lower-order schemes were derived based on the wave equation with periodic boundary conditions.

B. Non-periodic boundary conditions. The effect of numerical boundary schemes on the overall accuracy in computations of the wave equation with non-periodic boundary conditions is numerically tested. The non-periodic boundary condition is set at the left boundary as

$$u(0, t) = -\sin(\omega\pi t), \qquad t \geq 0. \tag{83}$$

TABLE II
L^1 Errors of Solving Wave Equation with Non-periodic Boundary Conditions

		e_1 errors		
ω	$L/\Delta x$	9-4-1-0 ($\alpha = 36$)	7-3-3-1 ($\alpha = 36$)	7-3-5-2 (Lele)
2	50.0	0.65 (−6)	0.54 (−6)	0.10 (−4)
$3\frac{1}{3}$	30.0	0.13 (−4)	0.10 (−4)	0.66 (−4)
$5\frac{1}{3}$	18.8	0.23 (−3)	0.18 (−3)	0.76 (−3)
$7\frac{1}{3}$	13.6	0.15 (−2)	0.12 (−2)	0.38 (−2)
$9\frac{1}{3}$	10.7	0.59 (−2)	0.53 (−2)	0.13 (−1)
$11\frac{1}{3}$	8.8	0.18 (−1)	0.17 (−1)	0.35 (−1)
$13\frac{1}{3}$	7.5	0.47 (−1)	0.45 (−1)	0.85 (−1)
$15\frac{1}{3}$	6.5	0.11	0.11	0.20
$17\frac{1}{3}$	5.8	0.26	0.28	0.54
$19\frac{1}{3}$	5.2	0.97	0.92	2.2

Note. The results correspond to test cases of different values of ω with a fixed number of grids $N = 50$ in a fixed computational domain (0, 1).

Similar to the previous case, the wave equation is solved in a fixed computational domain (0, 1) using 50 uniform grid points. Twenty runs are made using different values of ω so that the effects of grid resolution on the numerical errors of the scheme can be examined. The values of ω are chosen such that the computational domain is not a multiple of the wave length. The solutions are advanced in time in more than 10 periods for long time integration. The three inner schemes in the previous case are used with the following boundary closures: (1) explicit 5,5,5,5-7-5,5,5,5 boundary schemes for the 9-4-1-0 explicit inner scheme, (2) compact 5,5,6-7-6,5,5 boundary schemes for the 7-3-3-1 compact inner scheme, and (3) compact 4,4-4-4,4 boundary schemes for the spectral-like 7-3-5-2 compact inner scheme. The fourth-order boundary schemes are used because the inner scheme is fourth-order accurate and fifth-order boundary schemes are unstable.

Table II shows the errors of the numerical solutions using the three schemes with boundary closures. The results show that the seventh-order upwind compact and explicit schemes are much more accurate for small ω as expected. However, unlike the periodic case, as ω increases, the accuracy of the spectral-like scheme is about the same as the non-optimized schemes. For this test case, the schemes of formally higher order accuracy are more accurate in the computations of a range of wave modes. When there are less grid points in resolving the wave modes, the spectral-like schemes do not work as well mainly due to the effects of the boundary closures. Meanwhile, the errors of the seventh-order explicit upwind schemes (9-4-1-0) are only slightly larger than the corresponding upwind compact scheme (9-4-1-0).

C. Grid refinements on orders of accuracy. The formal orders of accuracy of the current upwind schemes are tested by computing the wave equation with a fixed $\omega = 2$ and three sets of grids: $N = 25, 50, 100$. For a global pth order scheme, the error should be reduced by a factor of 2^p times when grid size is reduced by half. The results are shown in Table III. The results in the table confirm the formal orders of accuracy of the schemes. The numerical stability also agrees with the eigenvalue analysis. The results also show that the accuracy of the boundary closure dominates the overall accuracy of the schemes. For the 3,4-6-4,3

TABLE III
L^1 Errors of Solving Wave Equation with Non-periodic Boundary Conditions Using Schemes with Numerical Boundary Closures

Inner schemes and B.C.'s		N	e_1	$e_1(N)/e_1(N/2)$
Inner	7-3-3-1 (Central, $\alpha = 0$)	25	0.97 (−3)	—
BC	3,4,4-6-4,4,3 compact	50	0.35 (−4)	28
Order	4	100	0.25 (−5)	14
Inner	7-3-5-2 (Central, Lele's Spectral-Like)	25	0.65 (−4)	—
BC	4,4,4-4-4,4,4 compact	50	0.10 (−4)	63
Order	4	100	0.33 (−6)	31
Inner	5-2-3-1 (Upwind, $\alpha = -1$)	25	0.11 (−3)	—
BC	4,4-5-4,4 compact	50	0.35 (−5)	32
Order	5	100	0.11 (−6)	32
Inner	7-3-1-0 (Upwind, $\alpha = -6$)	25	0.12 (−3)	—
BC	4,4,4-5-4,4,4 explicit	50	0.40 (−5)	31
Order	5	100	0.13 (−6)	31
Inner	7-3-3-1 (Upwind, $\alpha = 36$)	25	0.40 (−4)	—
BC	5,5,5-7-5,5,5 explicit	50	0.64 (−6)	63
Order	6	100	0.10 (−7)	64
Inner	9-4-1-0 (Upwind, $\alpha = 36$)	25	0.47 (−4)	—
BC	5,5,5,5-7-5,5,5,5 explicit	50	0.65 (−6)	73
Order	6	100	0.10 (−7)	64

Note. For each scheme, three sets of grids N are used in a fixed computational domain.

central compact scheme, the result is less accurate than the upwind 4,4-5-4,4 schemes because the central scheme is only third-order accurate.

Therefore, the numerical experiments on the linear wave equation confirm the accuracy and stability of the new high-order upwind schemes. The fourth-order spectral-like optimized compact scheme has better overall resolution than sixth-order upwind schemes for periodic problems. But the spectral-like scheme, which uses a wider grid stencil, is not as accurate as higher-order upwind schemes when boundary closure schemes are used in non-periodic computational domains. These results suggest that for non-periodic flow simulations, it is not worthwhile to lower the order of accuracy of the schemes in order to have better resolution at high wave numbers in the inner schemes, because boundary closure schemes cannot be included in the derivation of the optimized schemes.

Stability of 2-D Supersonic Couette Flow

Compressible Couette flow is a shear flow bounded by two parallel walls. While steady solutions are one-dimensional functions of wall-normal coordinate y, the amplification and decay of disturbances are two- and three-dimensional transient flows. The disturbance amplification or decay at finite Reynolds numbers can be analyzed by a normal-mode linear stability analysis, which solve for weak perturbations in the form

$$q' = \mathrm{Re}\left\{\hat{q}(y)\, e^{i(\alpha x - \omega t)}\right\}, \tag{84}$$

where q' represents perturbations of any flow variables, $\hat{q}(y)$ is the complex amplitude function of the perturbations, α is the wavenumber in x direction, and ω is the frequency of the disturbance waves. In the temporal linear stability analysis, ω is solved as an eigenvalue

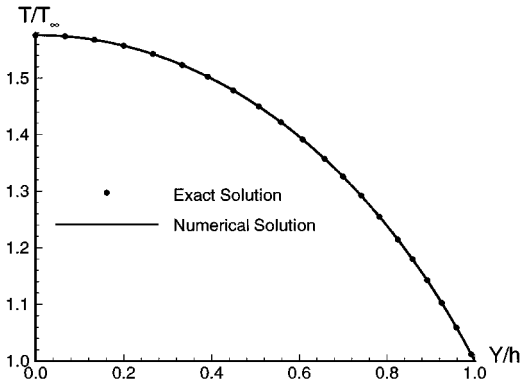

FIG. 11. Variation of the steady base flow temperature profile for adiabatic lower wall with $M_\infty = 2$. The numerical solution is obtained using a fifth-order upwind scheme using 121 grid points.

of the homogeneous boundary value problem for a given real value of α,

$$\omega = \omega(\alpha, \text{Re}, M_\infty). \tag{85}$$

The real part of ω, $\text{Re}\{\omega\}$, represents the frequency of the disturbance modes, while the imaginary part, $\text{Im}\{\omega\}$, represents the temporal amplification rate of the disturbances. When $\text{Im}\{\omega\}$ is greater, equal to, or smaller than 0, a disturbance mode is unstable with finite amplification, neutrally stable, or stable with finite damping, respectively.

In this section, the current fifth-order upwind schemes are used to compute supersonic Couette flow at $M_\infty = 2$ in solving the nonlinear Navier–Stokes equations for both steady and unsteady solutions. The unsteady numerical solutions are compared with the linear stability solutions of a supersonic Couette flow obtained by Hu and Zhong in [49]. The upper wall is an isothermal wall while the lower wall is an adiabatic wall. The gas is assumed to be a perfect gas with $\gamma = 1.4$ and $Pr = 0.72$. The viscosity coefficient is calculated using Sutherland's law. The flow variables are nondimensionalized by their corresponding values at the upper wall.

A. Steady flow solutions. The fifth-order explicit upwind schemes are used to compute the Navier–Stokes equations with $\alpha = -1$ for the supersonic Couette flow. The steady solutions are compared with analytical solutions obtained by a shooting method which is several order of magnitudes smaller in numerical errors [49]. The numerical simulation is conducted using several sets of uniform grids in order to evaluate the accuracy of the algorithm.

Figure 11 shows the steady temperature profile obtained by using a fifth-order upwind scheme with 121 uniform grid points. The numerical results agree well with the exact solutions. The numerical errors of the steady flow simulations using the three sets of grids are listed in Table IV. The numerical errors for the fifth-order upwind scheme are of the order of 10^{-6} using 31 grid points and 4.0×10^{-7} using 61 grid points. The theoretical ratio of the errors between the coarse and the fine grids is 32 for a fifth-order scheme. The numerical results in the table show that the numerical algorithms are able to maintain such high orders of accuracy.

B. Unsteady flow solutions. The fifth-order upwind scheme is applied to the unsteady supersonic Couette flow for the development of initial disturbances to the mean flow. The initial conditions are the steady flow solutions plus disturbances obtained by the linear

TABLE IV
Numerical Errors for Computations of Steady Supersonic Couette Flow Using a Fifth-Order Upwind Scheme for the Navier–Stokes Equations

Grids	α	$\|e\|_1$	Ratio	$\|e\|_2$	Ratio
31	-1	6.5 (-7)	—	1.7 (-7)	—
61	-1	2.4 (-8)	27	4.2 (-9)	40

stability analysis in the form of Eq. (84). The subsequent unsteady flow field is obtained by computing the nonlinear Navier–Stokes equations using the fifth-order upwind scheme. The same stretched grids as those used in the linear stability calculations [49] are used in the numerical simulations. The computational domain in the simulation is one period in length in the x direction. Periodic boundary conditions are used in the x direction. The Reynolds number is $Re_\infty = 1000$. The initial disturbance wave has a dimensionless wave number of $\alpha = 3$, and the eigenvalue obtained from the temporal linear stability analysis is

$$\omega = 5.52034015848 - 0.132786378788i, \tag{86}$$

where a negative Im$\{\omega\}$ means that the disturbances decay in time with a dimensionless frequency of Re$\{\omega\}$.

Figure 12 shows the time history of the velocity perturbations at a fixed point in the two-dimensional supersonic Couette flow. The DNS results are compared with the linear stability prediction. The computation uses a 40×100 grid. The figure shows that the instantaneous perturbations of the flow variables for the two-dimensional numerical simulations of the

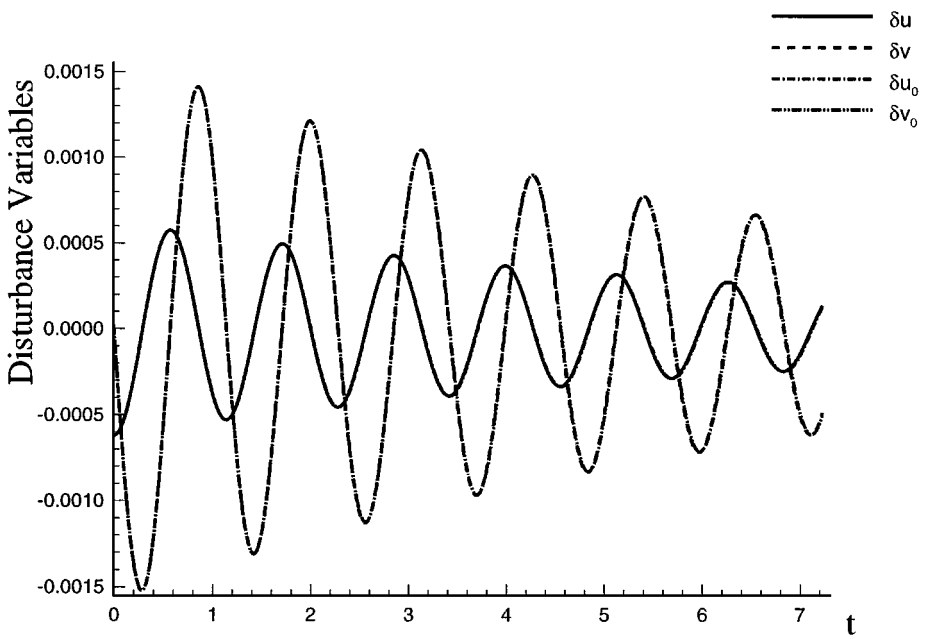

FIG. 12. Time history of velocity perturbations at a fixed point in the two-dimensional supersonic Couette flow field (linear stability theory, δu_0 and δv_0; DNS, δu and δv).

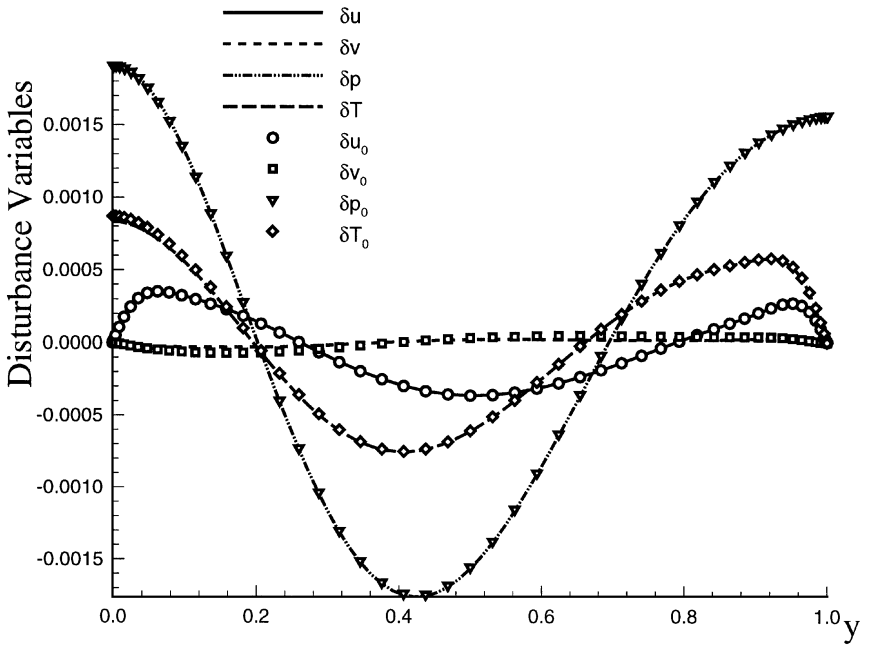

FIG. 13. Distribution of instantaneous flow perturbations in y direction in unsteady two-dimensional supersonic Couette flow.

nonlinear Navier–Stokes equations agree very well with the linear stability analysis. Figure 13 shows the distributions of instantaneous flow perturbations in the y direction at the end of about six periods in time. Again, the DNS results agree very well with the linear stability results. Grid refinements studies have also been performed and the results validate the fifth-order accuracy of the upwind scheme used in the calculations of the two-dimensional Navier–Stokes equations.

The amplitudes of the disturbance waves decay as a function of time. For sufficiently low amplitude waves, linear stability analysis shows that the perturbation kinetic energy of the solutions is

$$E(t) = \int\int \frac{1}{2}(u'^2 + v'^2)\, dx\, dy = E_0\, e^{2\omega_i t}, \tag{87}$$

where E_0 is the perturbation energy at $t = 0$. Figure 14 displays the time history of $\ln(E(t)/E_0)$ for the numerically computed perturbation energy and the analytical value of the linear stability analysis in one wave period. Different number of gridpoints in the y direction are used to study the numerical accuracy of the simulations. The numerical results using 100 gridpoints in the y direction agree very well with the linear stability results. However, the numerical errors are accumulated in time when lesser number of gridpoints, 30 and 20 gridpoints, are used in the y direction.

Steady Hypersonic Viscous Flow over a Cylinder

After validation without the shock-fitting procedure, the new fifth-order upwind scheme (7-3-1-0 with $\alpha = -6$) coupled with the shock-fitting procedure is then applied to the computations of steady two-dimensional hypersonic viscous flow over a cylinder, where there

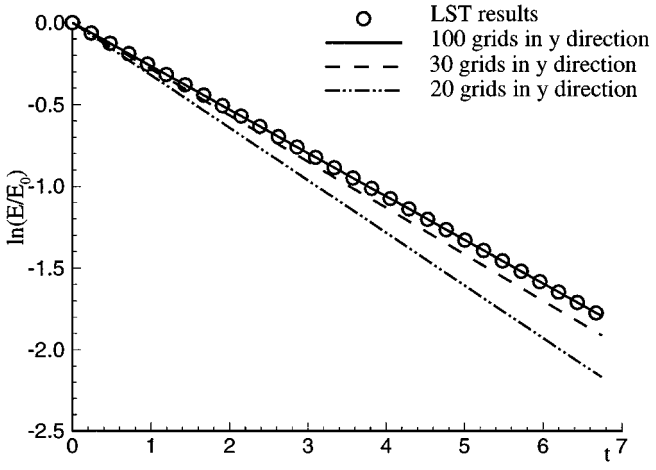

FIG. 14. Computed decay rate of perturbation energy for a fifth-order upwind scheme by using three sets of grids in the y direction compared with linear stability analysis results in 2-D supersonic Couette flow field ($M_\infty = 2.0$, $R_e = 1000$).

is a bow shock in front of the body. Experimental results and accurate numerical solutions obtained by a shock-fitting spectral method [50] are available for comparison. The flow conditions are $M_\infty = 5.73$, $Re_\infty = 2050$, $T_\infty = 39.6698$ K, $T_w = 210.02$ K, $\gamma = 1.4$, $Pr = 0.77$, and cylinder radius $r = 0.0061468$ m.

Figure 15 shows a set of 80×60 grids used in the shock-fitting calculations. The grids are stretched in both the streamwise and wall-normal directions. Figure 16 compares the computed temperature contours for flow over a circular cylinder. The results of the current fifth-order upwind shock-fitting scheme compare very well with those of the spectral

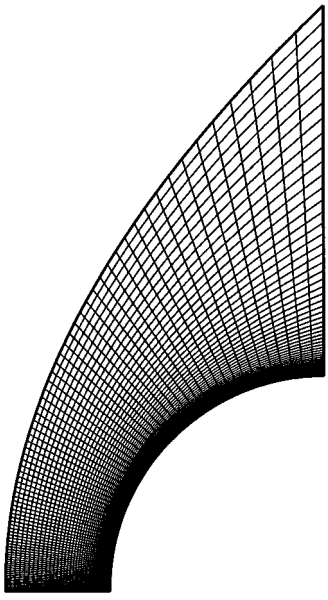

FIG. 15. Computational grid for viscous hypersonic flow over a circular cylinder.

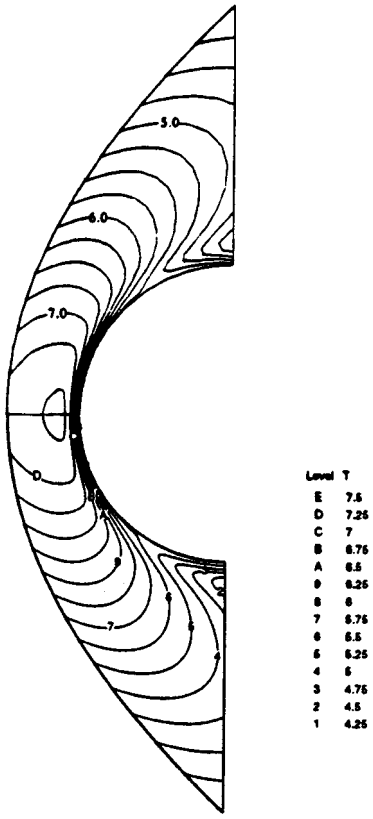

FIG. 16. Comparison of computed temperature contours for flow over a circular cylinder. The upper half contours are taken from Kopriva [50], and the lower half contours are computed by a fifth-order upwind shock-fitting scheme using a 80×60 grid.

method of Kopriva [50]. The pressure coefficients along the cylinder surface computed by the fifth-order shock-fitting methods are compared with experimental results and spectral results [50] in Fig. 17. Again, the solutions of the Navier–Stokes equations obtained by the current fifth-order upwind scheme agree well with the spectral-method results. The differences between the numerical results and the experiments, which are consistent with other numerical results, may be due to the differences in flow conditions between the experiments and the simulation. The grid convergence of the results are tested by refining the grids used for the simulation. Figure 18 compares the the surface pressure coefficients along the surface for three sets of grids and shows that the results are highly accurate for relatively coarse grids.

7. HYPERSONIC BOUNDARY-LAYER RECEPTIVITY SIMULATIONS

The new fifth-order upwind shock-fitting scheme (7-3-1-0 with $\alpha = -6$) is applied to the numerical simulation of boundary-layer receptivity to freestream acoustic disturbances for hypersonic flow past a parabolic leading edge at zero angle of attack. Perfect gas assumption is used for the flow. The hypersonic receptivity phenomena and the descriptions of the flow conditions of the simulations can be found in [51]. The fifth-order upwind shock-fitting scheme is used to discretize the equations in the non-periodic streamwise and wall-normal

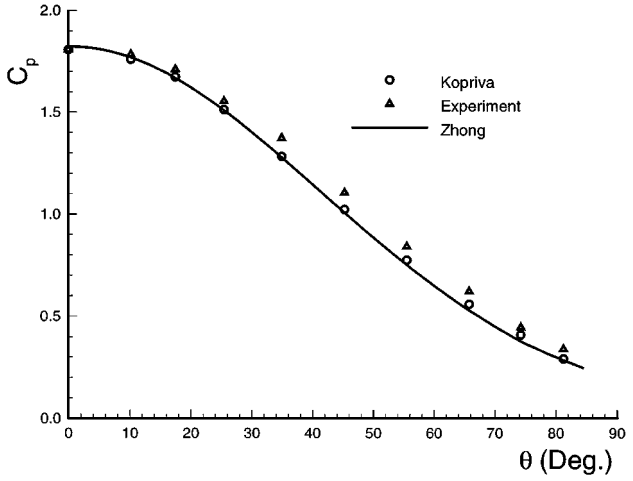

FIG. 17. Comparison of pressure coefficients along a cylinder surface.

directions. A Fourier spectral collocation method is used to discretize the equations in the periodic spanwise direction. In the shock-fitting algorithm, the derivatives of the shock shape H_ξ, H_ζ, $H_{\tau\xi}$, and $H_{\tau\zeta}$ are needed. They are numerically evaluated using a sixth-order compact central scheme shown in Eqs. (37) to (41). The spatially discretized equations are advanced in time using an explicit Runge–Kutta scheme [42] for the perfect gas flow. Grid refinements are used to ensure that both steady and unsteady solutions are grid independent.

In the simulations, two-dimensional steady flow solutions are first obtained with no freestream disturbances. Subsequently, the two-dimensional or three-dimensional freestream disturbances are superimposed on the basic flow solutions in front of the bow shock. The shock/disturbance interactions and generation of T-S waves in the boundary layer are simulated by solving the nonlinear Navier–Stokes equations in the two-dimensional or three-dimensional flow fields. The freestream disturbances are assumed to be weak monochromatic planar acoustic waves with wave front oblique to the center line of the

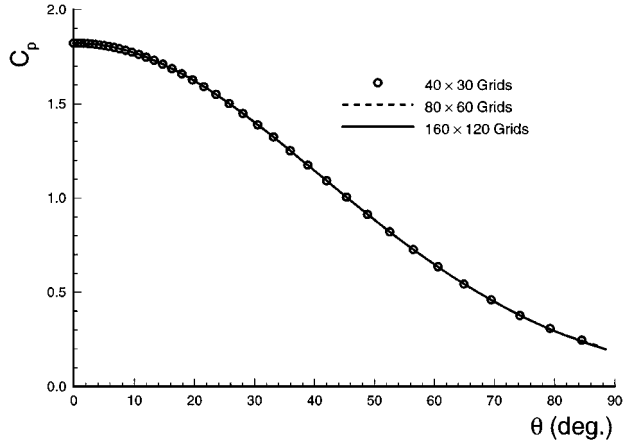

FIG. 18. Comparison of pressure coefficients along a cylinder surface. The results are obtained using three sets of grids.

body in the x-z plane. The perturbations of flow variables in the freestream introduced by the freestream acoustic waves before reaching the bow shock can be written in the form

$$q'_\infty = |q'|_\infty e^{i(k\cos\psi x + k\sin\psi z - \omega t)}, \tag{88}$$

where $|q'|$ represents one of the flow variables, $|u'|$, $|v'|$, $|w'|$, $|p'|$, and $|\rho'|$. Freestream acoustic perturbation amplitudes satisfy the following relations: $|u'|_\infty = \epsilon\cos\psi$, $|v'|_\infty = 0$, $|w'|_\infty = \epsilon\sin\psi$, $|p'|_\infty = \gamma M_\infty \epsilon$, and $|\rho'|_\infty = M_\infty \epsilon$. The parameter ϵ represents the freestream wave magnitude. The angle ψ is the angle of freestream wave with respect to the x axis in the x-z plane, where $\psi = 0$ corresponds to two-dimensional planar waves. The parameter k is the dimensionless freestream wave number which is related to the dimensionless circular frequency ω by $\omega = k(\cos\psi + M_\infty^{-1})$. The dimensionless frequency F is defined as $F = \omega^* \nu^* / U_\infty^{*2} \times 10^6$. The body surface is a parabola given by $x^* = b^* y^{*2} - d^*$, where b^* is a constant and d^* is taken as the reference length. A flow variable with a superscript $*$ is a dimensional variable, while dimensionless flow variables are denoted by the same dimensional notation but without the superscript $*$.

The flow and geometric conditions are $M_\infty = 15$, $Re_\infty = 6026.6$, $T_\infty^* = 192.989$ K, $p_\infty^* = 10.3$ Pa, $T_w^* = 1000$ K, $\gamma = 1.4$, $b^* = 40\ \mathrm{m}^{-1}$, $d^* = 0.1$ m, and the nose radius of curvature $r^* = 0.0125$ m. The body surface is assumed to be a non-slip wall with an isothermal wall temperature T_w^*.

Boundary conditions for flow variables at the wall surface, in the freestream, and in the exit boundary are needed for both steady and unsteady and unsteady flow simulations of the hypersonic receptivity problem. At the wall surface, the velocity is specified by the non-slip condition, the temperature is given by an isothermal condition, and the pressure is determined by a high-order polynomial extrapolation from the interior flow field. In the freestream, the steady or unsteady flow variables are specified in the calculations. The flow variables behind the bow shocks are then calculated without any linearization by the shock fitting algorithm described in this paper. At the exit boundary, the flow is supersonic outside of the boundary layer and is mainly parabolic inside the subsonic boundary layer. For such flow, a simple high-order polynomial extrapolation is used to determine the flow variables at the exit boundary. In order to ensure that such a boundary condition does not produce spurious reflection of numerical noise back to the upstream of the computational flow fields, the simulations of the steady and unsteady flow for the receptivity problem are carried out using two successive overlap computational zones similar to those shown in Fig. 28. The steady or unsteady solutions in Zone 1 are first computed until the solutions reach a steady state or time periodic state (for unsteady flows). Having finished the simulation in Zone 1, the simulations in Zone 2 are carried out using the solutions from Zone 1 as boundary conditions at the inlet. The use of the overlap-zone approach provides a way to evaluate the magnitudes of possible numerical wave reflection at the exit boundary. If there is no spurious numerical reflection at the exit boundary, the solutions from the two zones in the overlap region should agree with each other. The comparison of the results in the overlap region shows that the wave reflections at the exit boundary for the present test cases are negligible at the exit of Zone 1.

Steady Mean-Flow Solutions

Steady two-dimensional solutions of the Navier–Stokes equation for hypersonic flow over the parabola are obtained by advancing the solutions to a steady state without freestream

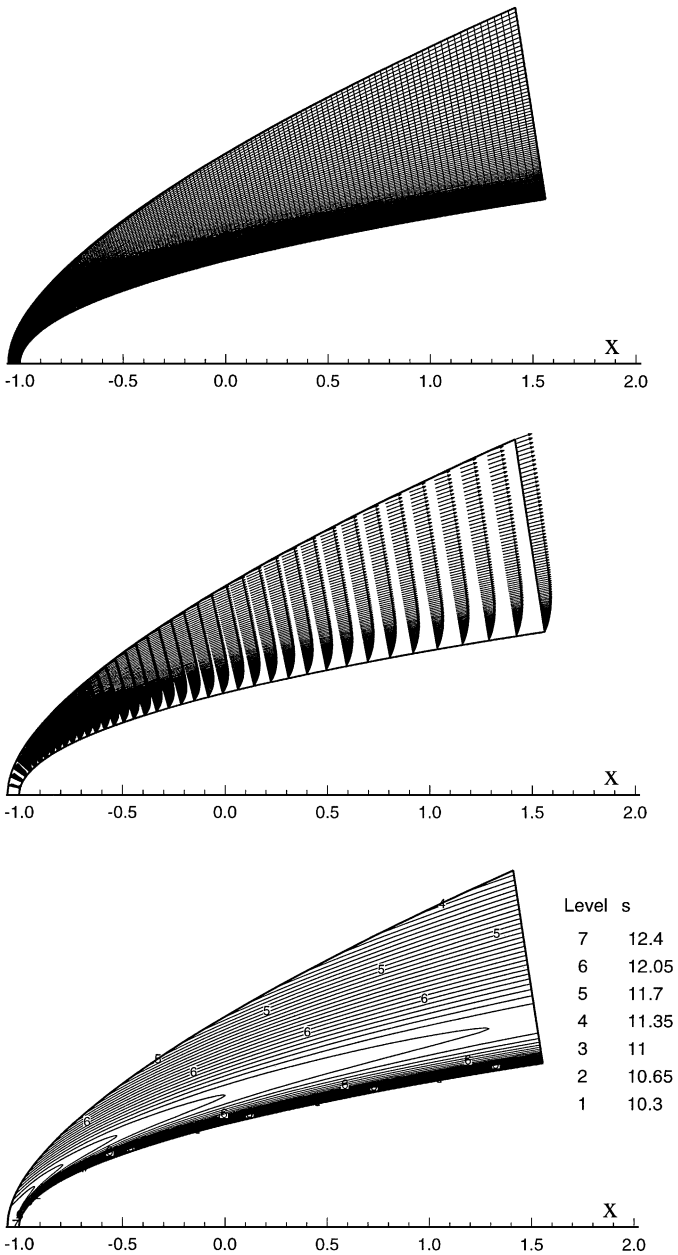

FIG. 19. Base flow solutions for a computational grid (upper figure) where the bow shock shape is obtained as the numerical solution for the freestream grid line, velocity vectors (middle figure), and entropy contours (lower figure).

perturbations. Figure 19 shows steady flow solutions for a set of 160×120 computational grid, velocity vectors, and steady entropy contours. The bow shock is obtained as the solution for the freestream grid line. The velocity vector plot in the figure shows the development of the boundary layer along the surface. The entropy contours show the entropy layer developing at the edge of the boundary layer. The swallowing of the entropy layer by the boundary layer has been shown to play an important role in the stability and transition of the boundary layer downstream [12].

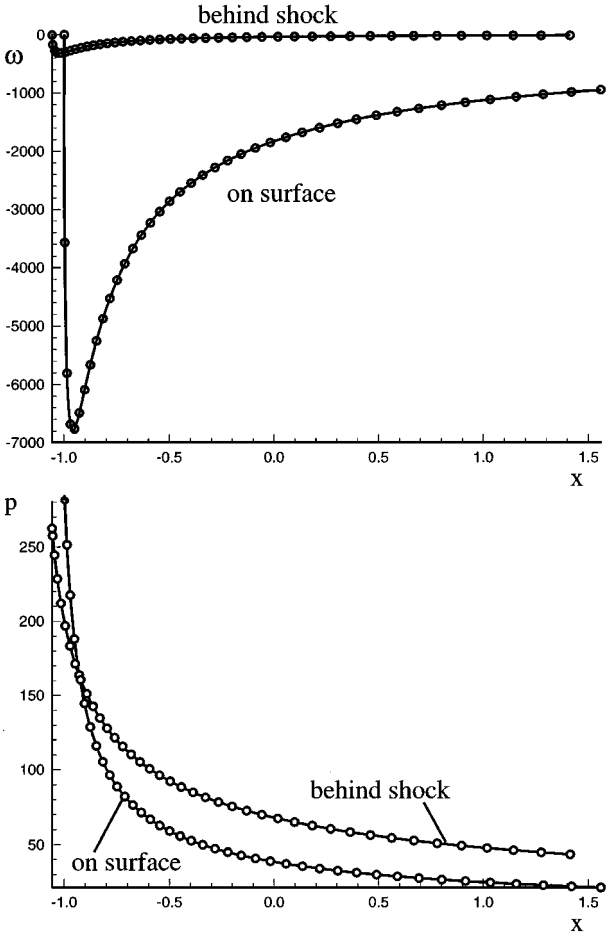

FIG. 20. Comparisons of steady pressure (p) and vorticity (ω) profiles behind the bow shock and on body surface obtained by two set of grids (circles, 160×120 grid; lines, 320×240 grid).

The accuracy of the numerical resolution of the mean flow using the 160×120 grid is evaluated by comparison with finer 320×240 grid solutions. Figure 20 compares the pressure and vorticity profiles behind the bow shock shape and on the body surface. The two sets of solutions agree very well with each other, which indicates that the steady solutions are well resolved by these grids.

Boundary layer stability is strongly dependent on the variation of steady flow temperature and velocities along the wall-normal grid lines, and their first and second derivatives. Figure 21 shows the variation of base flow tangential nondimensional velocity (u), its first derivative ($\frac{du}{dy}$), and second derivative ($\frac{d^2u}{dy^2}$) along a grid line normal to the parabola surface at a grid station. The grid refinements show that these steady solutions are grid independent. This figure also shows that the flow distribution across the boundary layer for the present test case is very different from a hypersonic boundary layer over a flat plate. Specifically, the velocities do not reach constant asymptotic states outside the boundary layer. Therefore, it is expected that the stability properties will be different from those obtained from a LST analysis which is based on parallel base flow assumptions.

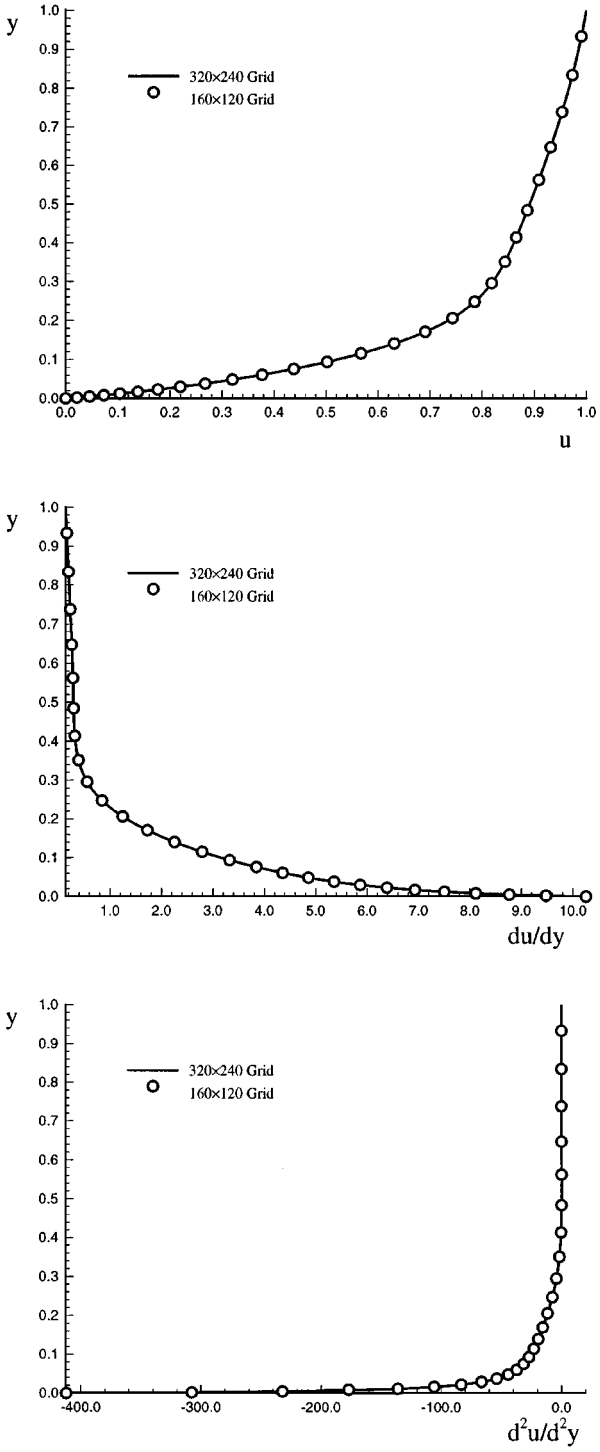

FIG. 21. Variation of base flow tangential velocity (u), its first derivative ($\frac{du}{dy}$), and second derivative ($\frac{d^2u}{dy^2}$) along a grid line normal to the wall surface at the $x = -0.14$ grid station.

Receptivity to 2-D Disturbance Waves

After obtaining the steady basic flow solutions, the unsteady flow solutions are computed using the new fifth-order upwind scheme by imposing acoustic disturbances to the basic flow in the freestream. Figure 22 shows the contours of instantaneous temperature perturbation T', the Fourier amplitude $|T'|$, and the phase angle φ_T after the solutions reach a periodic state for the case of freestream forcing frequencies of $F = 2655$ and $\epsilon = 5 \times 10^{-4}$. The numerical solutions are obtained by using the 160×120 grids. The instantaneous contours show the development of instability waves in the boundary layer on the surface. In general, the disturbance field between the shock and the body surface is a combination of the external forcing disturbance waves and the T-S waves generated in the boundary layer. Figure 22 shows very clearly the development of instability waves in the boundary layer along the surface because the instability waves are dominant in the boundary layer near the surface. Meanwhile the waves immediately behind the bow shock are mainly external forcing waves. On the body surface, both first and second mode waves are generated and propagated downstream along the wall. The first mode is generated near the leading edge ($x < 0.2$). The amplitudes of the first mode are amplified first and then decrease rapidly after reaching maximum values. After the first-mode decay, the second-mode disturbances become the dominant mode. The decay of the first mode and the growth of the second mode at $x \approx 0.2$ are shown by a sudden change of phase angles near the body surface at that location. The phase structure changes dramatically between the two modes; specifically the second mode has one more variation across the boundary layer. The phase angle structure develops discontinuity lines across the boundary layer as the higher modes develop. The contours of the Fourier amplitudes also show the switching of instability modes from region 1 to region 2 at about $x = 0.2$ on the surface.

Again, a grid refinement is used to check the numerical resolution of the 160×120 grids for unsteady DNS simulations. Figure 23 shows the distribution of the Fourier amplitudes of the entropy perturbations along the body surface. The two distinct main regions of instability waves are clearly shown. The variation of perturbation amplitudes of velocity $|u'|$ along a grid line normal to parabola surface at $x = 0.239$ is shown in Fig. 24. These two figures show that the unsteady solutions obtained by using two sets of grids, 320×240 and 160×120 grids, agree very well with each other. The unsteady solutions are well resolved by the grids used in the calculations.

Local linear stability theory (LST) is used to identify the boundary layer eigenmodes and to analyze the instability mechanism and the bow-shock effects [52]. The LST is used to obtain instability modes based on the numerically obtained basic flow between the body and the bow shock. Figure 25 shows the first-mode eigenfunction amplitudes along the wall-normal direction at $x = 0.5521$ for the case of freestream forcing frequency $F = 1770$ and $\epsilon = 5 \times 10^{-4}$. The DNS results agree very well with LST results inside the boundary layer. The disagreement outside the boundary layer near the bow shock is expected because the effects of the forcing disturbances are not included in the linear stability analysis.

For weak monochromatic freestream forcing waves, the generation of instability waves is expected to be linear with respect to the forcing amplitudes. Receptivity and stability experiments [9] have shown the existence of high harmonics in addition to the waves of the fundamental frequency. Nonlinear higher harmonics are also found in the present DNS studies. Figure 26 shows the instantaneous entropy disturbances along the body surface for

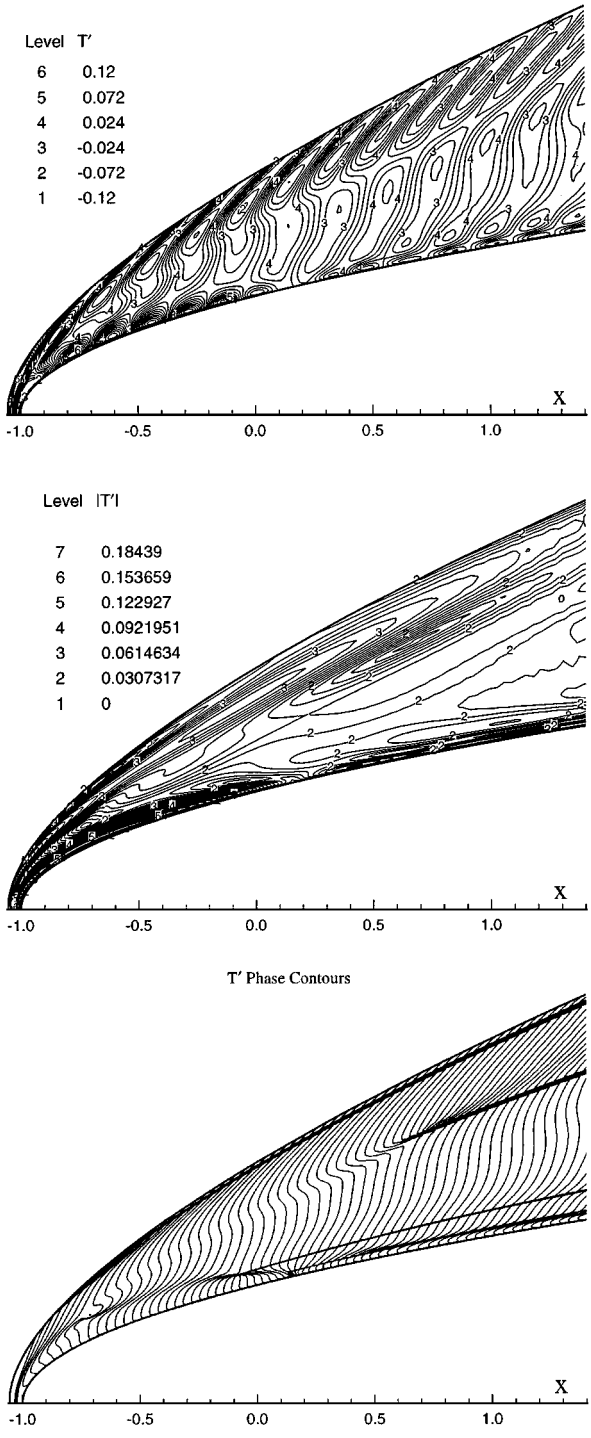

FIG. 22. Unsteady temperature perturbation contours for the case of 2-D freestream acoustic wave of $F = 2655$: instantaneous perturbations T' (upper figure), Fourier amplitude $|T'|$ (middle figure), and Fourier phase angle φ_T (in degrees) (lower figure).

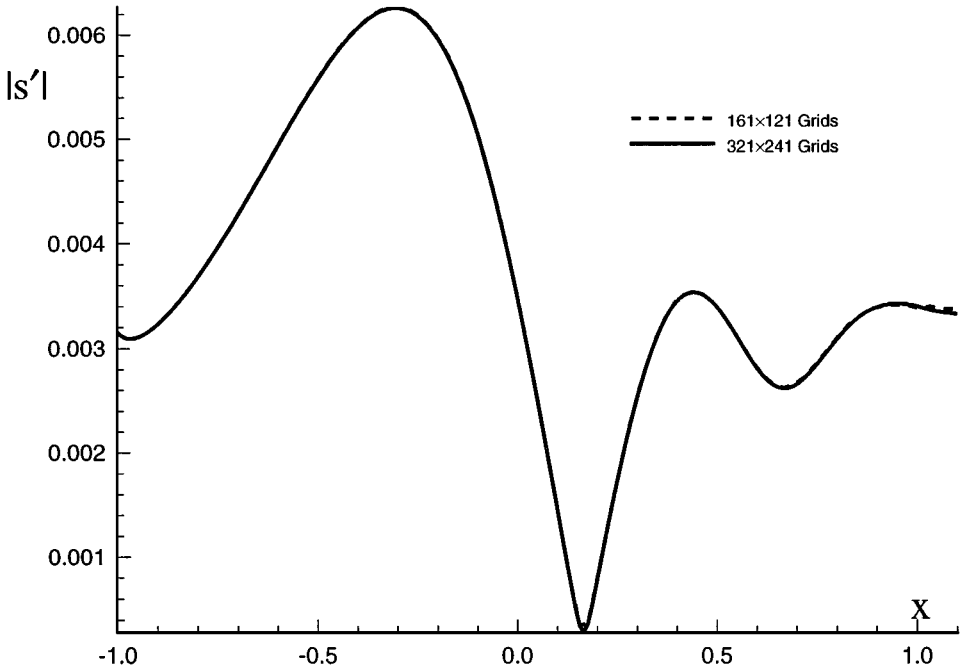

FIG. 23. Unsteady flow solutions at $F = 2655$ for the distribution of the amplitudes of the entropy perturbations along the body surface.

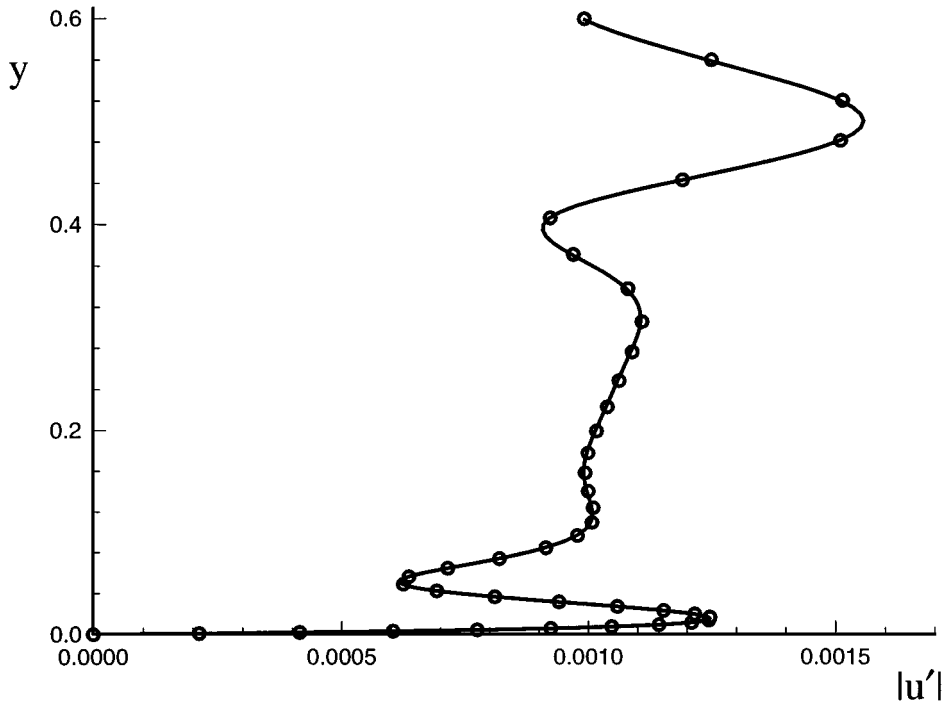

FIG. 24. Unsteady flow solutions for the case of $F = 2655$ for variation of $|u'|$ along a grid line normal to parabola surface at $x = 0.239$ (line, 320×240 grid; circles, 160×120 grid).

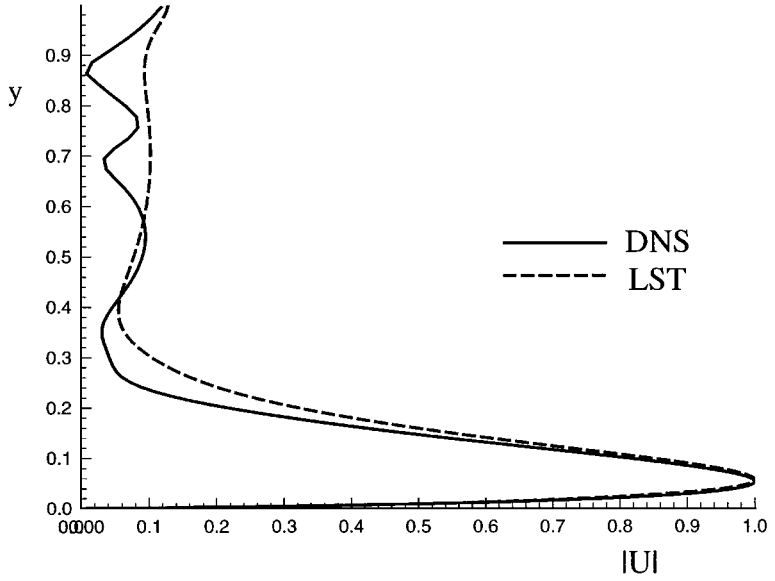

FIG. 25. First-mode eigenfunction amplitudes along the wall-normal direction at $x = 0.5521$ ($F = 1770$).

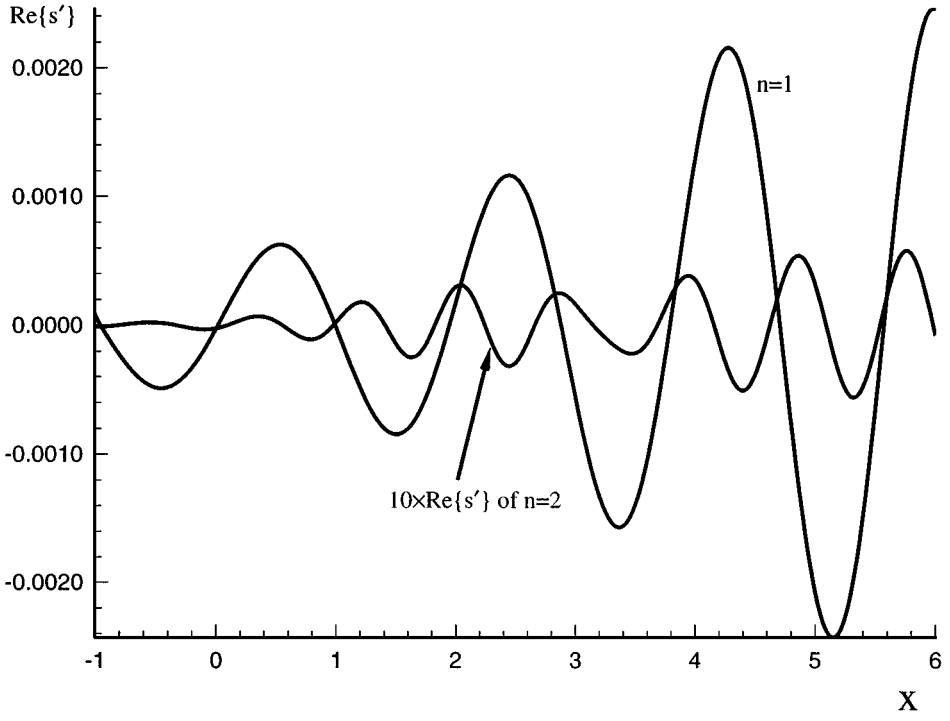

FIG. 26. Instantaneous entropy disturbances along the body surface for the case of $F = 1770$ ($n = 1$, fundamental mode; $n = 2$, second harmonic).

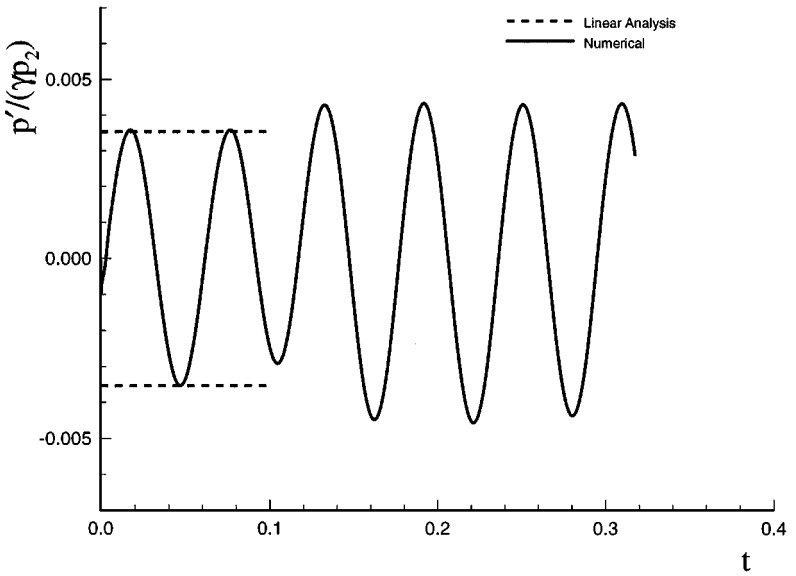

FIG. 27. Time history of the instantaneous pressure perturbation at the point immediately behind the bow shock at the center line for the case of $k = 40$.

the case of $F = 1770$ and $\epsilon = 5\times10^{-4}$ for the fundamental frequency ($n = 1$) and their second harmonic ($n = 2$). The analysis of the results shows that receptivity of the fundamental modes is governed by a linear mechanism, while the second harmonic is nonlinear.

In the unsteady simulations, the bow shock oscillates due to freestream disturbances and the reflection of acoustic waves from the boundary layer to the shock. It is important that the numerical simulation using the shock-fitting scheme resolves the unsteady shock motion accurately. The current high-order shock-fitting method is found to be able to compute the unsteady flow fields and the unsteady shock motion very accurately. A simple way to check the accuracy of the numerically computed unsteady shock/disturbances interaction by the shock-fitting scheme is shown in Fig. 27, which shows the time history of the instantaneous pressure perturbation at the point immediately behind the bow shock at the center line for the case of $k = 40$. In the initial moment of imposing the freestream disturbances, there are no reflected waves from the undisturbed steady boundary layer. The freestream disturbance wave transmission relation can be predicted by linear theory such as that derived by Mckenzie and Westphal [53]. At a later time, the wave pattern changes because the disturbance waves enter the boundary layer and generate reflected waves back to the shock. The figure shows very good agreement between DNS and linear predictions on the pressure perturbation due to freestream disturbances.

Receptivity to 3-D Disturbance Waves

The receptivity of the hypersonic boundary layer to oblique three-dimensional freestream acoustic waves for the same two-dimensional basic flow has also been studied by DNS. Figure 28 shows the three-dimensional shock fitted grids using two computational zones resolved by $160 \times 120 \times 16$ and $200 \times 120 \times 16$ grids, respectively. The unsteady flow fields are generated by imposing an oblique freestream disturbance at an angle of $\psi = 45^\circ$ with wave amplitude of $\epsilon = 5 \times 10^{-3}$ and $F = 1770$. Figure 29 shows the contours of

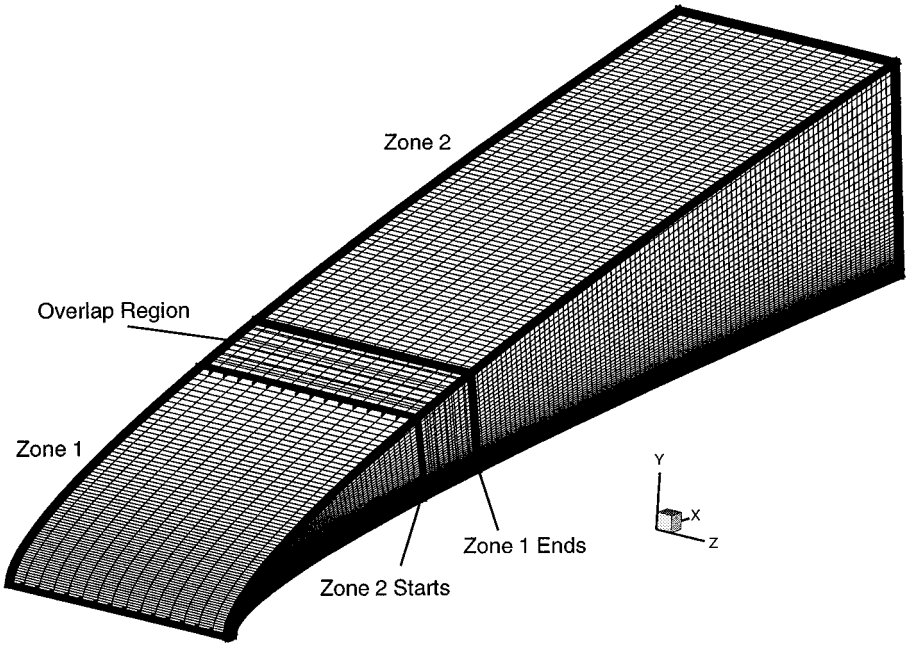

FIG. 28. Computational grid for three-dimensional hypersonic boundary layer receptivity to freestream oblique disturbance waves using two overlap zones.

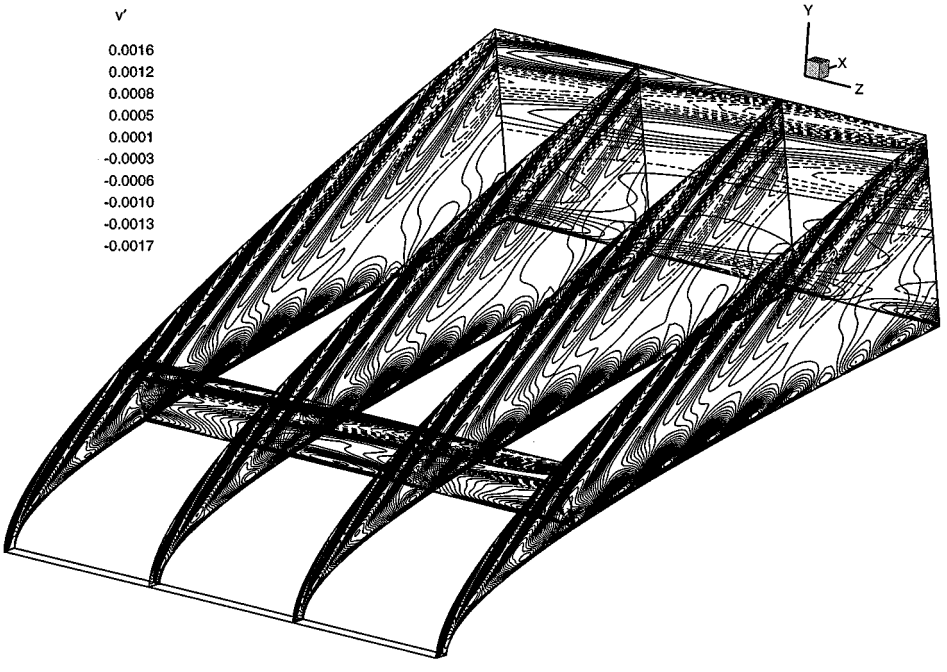

FIG. 29. Instantaneous v' contours for the receptivity to freestream disturbances for a three-dimensional hypersonic boundary layer over a parabolic leading edge.

instantaneous perturbation v' after the flow field reaches a periodic state. The instantaneous contours of v' show the development of three-dimensional first-mode waves in the boundary layer on the surface. The second mode region is also generated near the end of computational Zone 1. The figure shows similar trends as two-dimensional wave developments, i.e., the first-mode amplification near the leading edge and the second-mode dominant downstream.

8. CONCLUSIONS

This paper has presented a family of high-order compact and explicit upwind finite-difference schemes and a shock-fitting method for the DNS of hypersonic flows over blunt bodies. The accuracy and the stability of the schemes have been tested and applied to numerical simulations of the linear wave equation and nonlinear Navier–Stokes equations. The numerical experiments and applications have shown that the current high-order shock-fitting schemes are highly accurate for hypersonic boundary layer DNS studies. Specific conclusions are listed below.

(1) The numerical experiments confirm the accuracy and stability of the current high-order upwind schemes. They are stable with high-order boundary closure schemes and their dissipation errors are smaller than conventional upwind schemes using upwind-bias stencils.

(2) The new fifth-order shock-fitting schemes have been applied to the DNS studies of the receptivity of a hypersonic boundary layer to freestream acoustic disturbances. It is found that both first and second mode waves are generated in the hypersonic boundary layers. The first mode is always generated near the leading edge and is amplified before decaying rapidly. The second mode is the dominant mode after the first mode decay. The eigenfunctions of the first mode obtained by DNS agree well with the LST results. The DNS also shows that the generation of instability modes of the fundamental forcing frequency are linear, and the receptivity also generates nonlinear superharmonics.

(3) As a byproduct of the numerical experiments, a fourth-order spectral-like central compact scheme has also been compared with current upwind schemes. It is found that the spectral-like compact scheme has better overall resolution than sixth-order upwind schemes for periodic problems. But the spectral-like scheme is not as accurate as higher-order non-optimized schemes when boundary closure schemes are used in non-periodic computational domains.

APPENDIX: OTHER UPWIND SCHEMES

Third-Order Compact Schemes

$$b_{i-1}u'_{i-1}+b_iu'_i+b_{i+1}u'_{i+1}=\frac{1}{h}(a_{i-1}u_{i-1}+a_iu_i+a_{i+1}u_{i+1})-\frac{\alpha}{4!}h^3\left(\frac{\partial u^4}{\partial^4 x}\right)_i+\cdots, \quad (89)$$

where $a_{i\pm1}=\pm45-30\alpha$, $b_{i\pm1}=15\mp15\alpha$, $a_i=60\alpha$, and $b_i=60$. The 3-1-3-1 schemes are third-order upwind when $\alpha>0$, and are fourth-order central when $\alpha=0$. The recommended value for α is $\alpha=1/4$.

Third-Order Explicit Schemes

$$u'_i=\frac{1}{hb_i}\sum_{k=-2}^{2}a_{i+k}u_{i+k}-\frac{\alpha}{4!b_i}h^3\left(\frac{\partial u^4}{\partial^4 x}\right)_i+\cdots, \quad (90)$$

where $a_{i\pm2} = \mp 5 + \frac{5}{2}\alpha$, $a_{i\pm1} = \pm 40 - 10\alpha$, $a_i = 15\alpha$, and $b_i = 60$. The 5-2-1-0 schemes are third-order upwind when $\alpha > 0$, and they are fourth-order central when $\alpha = 0$. The recommended value for α is $\alpha = 1/4$.

Seventh-Order Compact Schemes

$$b_{i-1}u'_{i-1} + b_i u'_i + b_{i+1}u'_{i+1} = \frac{1}{h}\sum_{k=-3}^{3} a_{i+k}u_{i+k} - \frac{\alpha}{8!}h^7\left(\frac{\partial u^8}{\partial^8 x}\right)_i + \cdots, \tag{91}$$

where $a_{i\pm3} = \mp\frac{1}{8} + \frac{1}{96}\alpha$, $a_{i\pm2} = \pm 3 - \frac{1}{6}\alpha$, $a_{i\pm1} = \pm\frac{375}{8} - \frac{65}{96}\alpha$, $b_{i\pm1} = \frac{45}{2} \mp \frac{5}{8}\alpha$, $a_i = \frac{5}{3}\alpha$, and $b_i = 60$. These 7-3-3-1 schemes are seventh-order upwind compact schemes when $\alpha > 0$, and are a eighth-order central compact scheme when $\alpha = 0$. The recommended value for α is $\alpha = 36$.

Seventh-Order Explicit Schemes

$$u'_i = \frac{1}{hb_i}\sum_{k=-4}^{4} a_{i+k}u_{i+k} - \frac{\alpha}{8!b_i}h^7\left(\frac{\partial u^8}{\partial^8 x}\right)_i + \cdots, \tag{92}$$

where $a_{i\pm4} = \mp\frac{3}{14} + \frac{1}{672}\alpha$, $a_{i\pm3} = \pm\frac{16}{7} - \frac{1}{84}\alpha$, $a_{i\pm2} = \mp 12 + \frac{1}{24}\alpha$, $a_{i\pm1} = \pm 48 - \frac{1}{12}\alpha$, $a_i = \frac{5}{48}\alpha$, and $b_i = 60$. These 9-4-1-0 schemes are seventh-order upwind explicit schemes when $\alpha > 0$, and are a eighth-order central explicit scheme when $\alpha = 0$. The recommended value for α is $\alpha = 36$.

For the seventh-order upwind compact (7-3-3-1) and explicit (9-4-1-0) schemes, it is desirable that the boundary schemes are sixth-order accurate so that the overall schemes are seventh-order accurate. However, the required damping parameters α for stability are too large (in the range of 10^4) for both schemes. Such large values of α will lead to very large numerical dissipation errors. Therefore, the requirement of the order of boundary schemes for the seventh-order inner schemes is reduced to fifth-order in order to obtain stable boundary closure at reasonable value of damping coefficient α. The corresponding schemes are 5,5,5-6-5,5,5 for compact schemes and 5,5,5,5-6-5,5,5,5 for explicit schemes. The formal global order of accuracy of the seventh-order interior schemes with fifth-order boundary closure are formally sixth-order accurate. The upwind schemes are stable with $\alpha = 36$ for both schemes.

ACKNOWLEDGMENTS

This research was supported by the Air Force Office of Scientific Research under Grants F49620-94-1-0019 and F 49620-95-1-0405 monitored by Dr. Len Sakell. Some of the results presented in this paper were presented in the 35th AIAA Aerospace Sciences Meeting and Exhibit, January 6–9, 1997, Reno, Nevada, as AIAA Paper No. 97-0755. The author thanks Mr. Yanbao Ma for providing Figs. 7–9 and Mr. Haibo Dong for providing Fig. 14 in the paper.

REFERENCES

1. Defense Science Board, *Final Report of the Second Defense Science Board Task Force on the National Aero-Space Plane (NASP)*, AD-A274530, 94-00052, November 1992.
2. T. Herbert and M. V. Morkovin, Dialogue on bridging some gaps in stability and transition research, in *Laminar-Turbulent Transition, IUTAM Symposium, Stuttgart, Germany*, edited by R. Eppler and H. Fasel (Springer-Verlag, Berlin, 1980), p. 47.

3. M. V. Morkovin and E. Reshotko, Dialogue on progress and issues in stability and transition research, in *Laminar-Turbulent Transition, IUTAM Symp., Toulouse*, edited by D. Arnal and R. Michel (Springer-Verlag, Berlin, 1990), p. 3.
4. M. Morkovin, On the many faces of transition, in *Viscous Drag Reduction*, edited by C. Wells (Plenum, New York, 1969), p. 1.
5. W. S. Saric, H. L. Reed, and E. J. Kerschen, *Leading Edge Receptivity to Sound: Experiments, DNS, and Theory*, AIAA Paper 94-2222, 1994.
6. L. M. Mack, *Boundary Layer Linear Stability Theory*, AGARD Report, No. 709, pp. 3–1 to 3–81, 1984.
7. W. S. Saric, Götler vortices, *Ann. Rev. Fluid Mech.* **26**, 379 (1994).
8. H. L. Reed and W. S. Saric, Stability of three-dimensional boundary layers, *Ann. Rev. Fluid Mech.* **21**, 235 (1989).
9. K. F. Stetson and R. L. Kimmel, *On Hypersonic Boundary Layer Stability*, AIAA Paper 92-0737, 1992.
10. Y. S. Kachanov, Physical mechanisms of laminar-boundary-layer transition, *Ann. Rev. Fluid Mech.* **26**, 411 (1994).
11. L. S. G. Kovasznay, Turbulence in supersonic flow, *J. Aeronaut. Sci.* **20**(10), 657 (1953).
12. E. Reshotko and N. M. S. Khan, Stability of the laminar boundary layer on a blunt plate in supersonic flow, in *IUTAM Symposium on Laminar-Turbulent Transition*, edited by R. Eppler and H. Fasel (Springer-Verlag, Berlin, 1980), p. 186.
13. L. Kleiser and T. A. Zang, Numerical simulation of transition in wall-bounded shear flows, *Ann. Rev. Fluid Mech.* **23**, 495 (1991).
14. L. Klerser and E. Laurien, *Numerical Investigation of Interactive Transition Control*, AIAA Paper 85-0566, 1985.
15. T. A. Zang and M. Y. Hussaini, *Numerical Experiments on Subcritical Transition Mechanisms*, AIAA Paper 81-1227, 1981.
16. H. Fasel, Investigation of the stability of boundary layers by a finite difference model of the Navier–Stokes equations, *J. Fluid Mech.* **78**, 355 (1976).
17. U. Rist and H. Fasel, Direct numerical simulation of controlled transition in flat-plate boundary layer, *J. Fluid Mech.* **298**, 211 (1995).
18. M. M. Rai and P. Moin, Direct numerical simulation of transition and turbulence in a spatially evolving boundary layer, *J. Comput. Phys.* **109**, 169 (1993).
19. G. Danabasoglu, S. Biringen, and C. L. Strett, *Spatial Simulation of Boundary Layer Instability: Effects of Surface Roughness*, AIAA Paper 93-0075, 1993.
20. H. Bestek, M. Kloker, and W. Muller, Spatial direct numerical simulation of boundary layer transition under adverse pressure gradient, in *Application of Direct and Large Eddy Simulation to Transition and Turbulence* (AGARD-CP-551, 1994).
21. R. D. Joslin, C. L. Strett, and C.-L. Chang, Spatial direct numerical simulation of boundary-layer transition mechanisms: Validation of PSE theory, *Theoret. Comput. Fluid Dynam.* **4**, 271 (1993).
22. G. Erlebacher and M. Y. Hussaini, Numerical experiments in supersonic boundary-layer stability, *Phys. Fluids A* **2**, 94 (1990).
23. L. L. Ng and G. Erlebacher, Secondary instability in compressible boundary layers, *Phys. Fluids A* **4**, 710 (1992).
24. A. Thumm, W. Wolz, and H. Fasel, Numerical simulation of spatially growing three-dimensional disturbance waves in compressible boundary layers, in *Laminar-Turbulent Transition, IUTAM Symposium, Toulouse, France, 1989*, edited by D. Arnal and R. Michel (Springer-Verlag, Berlin, 1990), p. 303.
25. W. Eibler and H. Bestek, Spatial numerical simulations of linear and weakly nonlinear instabilities in supersonic boundary layers, *Theoret. Comput. Fluid Dynam.* **8**, 219 (1996).
26. N. A. Adams and L. Kleiser, Subharmonic transition to turbulence in a flat-plate boundary layer at mach number 4.5, *J. Fluid Mech.* **317**, 301 (1996).
27. Y. Guo, N. A. Adams, N. D. Sandham, and L. Kleiser, Numerical simulation of supersonic boundary layer transition, in *Application of Direct and Large Eddy Simulation to Transition and Turbulence* (AGARD-CP)-551, 1994).

28. C. D. Pruett and T. A. Zang, Direct numerical simulation of laminar breakdown in high-speed axisymmetric boundary layers, *Theoreti. Comput. Fluid Dynam.* **3**, 345 (1992).
29. C. D. Pruett, T. A. Zang, C.-L. Chang, and M. H. Carpenter, Spatial direct numerical simulation of high-speed boundary-layer flows. Part I. Algorithmic considerations and validation, *Theoret. Comput. Fluid Dynam.* **7**, 49 (1995).
30. X. Zhong, Additive semi-implicit Runge–Kutta schemes for computing high-speed nonequilibrium reactive flows, *J. Comput. Phys.* **128**, 19 (1996).
31. A. T. Patera, A spectral element method for fluid dynamics: Laminar flow in a channel expansion, *J. Comput. Phys.* **54**, 468 (1984).
32. S. K. Lele, Compact finite difference schemes with spectral-like resolution, *J. Comput. Phys.* **103**, 16 (1992).
33. M. H. Carpenter, D. Gotlieb, and S. Abarbanel, The stability of numerical boundary treatments for compact high-order finite-difference schemes, *J. Comput. Phys.* **108**, 272 (1993).
34. A. I. Tolstykh, On a class of noncentered compact difference schemes of fifth order, based on Pade approximants, *Soviet Math. Dokl.* **44**(1), 69 (1991).
35. I. Christie, Upwind compact finite difference schemes, *J. Comput. Phys.* **59**, 353 (1985).
36. D. W. Zingg, H. Lomax, and H. Jurgens, High-accuracy finite-difference schemes for linear wave propagation, *SIAM J. Sci. Comput.* **17**(2), 328 (1995).
37. B. Sjögreen, High order centered difference methods for the compressible Navier–Stokes equations, *J. Comput. Phys.* **117**, 67 (1995).
38. N. A. Adams and K. Shariff, A high-resolution hybrid compact-ENO scheme for shock-turbulence interaction problems, *J. Comput. Phys.* **127**, 27 (1996).
39. A. Harten, B. Engquist, S. Osher, and S. Chakravarthy, Uniformly high order accurate essentially non-oscillatory schemes, III, *J. Comput. Phys.* **71**, 231 (1987).
40. M. Y. Hussaini, D. A. Kopriva, M. D. Salas, and T. A. Zang, Spectral methods for the Euler equations. Part II. Chebyshev methods and shock fitting, *AIAA J.* **23**(1), 234 (1985).
41. W. Cai, High-order hybrid numerical simulations of two-dimensional detonation waves, *AIAA J.* **33**(7), 1248 (1995).
42. J. H. Williamson, Low-storage Runge–Kutta schemes, *J. Comput. Phys.* **35**, 48 (1980).
43. G. H. Furumoto, X. Zhong, and J. C. Skiba, Numerical studies of real-gas effects on two-dimensional hypersonic shock-wave/boundary-layer interaction, *Phys. Fluids* **9**(1), 191 (1997).
44. B. Gustafsson, H.-O. Kreiss, and A. Sundstrom, Stability theory of difference approximations for mixed initial boundary value problems, II, *Math. Comput.* **26**(119), 649 (1972).
45. G. O. Roberts, Computational meshes for boundary layer problems, in *Proc. Second International Conf. Numerical Methods Fluid Dyn.*, Lecture Notes in Physics (Springer-Verlag, New York, 1971), Vol. 8, p. 171.
46. J. J. Yoh and X. Zhong, *Computations of Multi-Dimensional Detonation Using Semi-Implicit Runge–Kutta Schemes*, AIAA Paper 97-0803, January 1997.
47. C. K. W. Tam and J. C. Webb, Dispersion-relation-preserving finite difference schemes for computational acoustics, *J. Comput. Phys.* **107**, 262 (1993).
48. Z. Haras and S. Ta'asan, Finite difference schemes for long-time integration, *J. Comput. Phys.* **114**, 265 (1994).
49. S. H. Hu and X. Zhong, *Linear Stability of Compressible Couette Flow*, AIAA Paper 97-0432, January 1997.
50. D. A. Kopriva, Spectral solution of the viscous blunt body problem, *AIAA J.* **31**(7), 1235 (1993).
51. X. Zhong, *Direct Numerical Simulation of Hypersonic Boundary-Layer Transition Over Blunt Leading Edges. Part II. Receptivity to Sound (Invited)*, AIAA Paper 97-0756, January 1997.
52. S. H. Hu and X. Zhong, *Linear Stability of Hypersonic Flow over a Parabolic Leading Edge*, AIAA Paper 97-2015, July 1997.
53. J. F. Mckenzie and K. O. Westphal, Interaction of linear waves with oblique shock waves, *Phys. Fluids* **11**(11), 2350 (1968).